Offset-free Nonlinear Model Predictive Control for Improving Dynamics of Cable-Driven Parallel Robots with On-board Thrusters

Loïc Cuvillon, Miguel Arpa Perozo, Arda Yiğit, Sylvain Durand, Jacques Gangloff

Offset-free Nonlinear Model Predictive Control for Improving Dynamics of Cable-Driven Parallel Robots with On-board Thrusters

Loïc Cuvillon[a,*], Miguel Arpa Perozo[a], Arda Yiğit[a], Sylvain Durand[a,b], Jacques Gangloff[a]

[a] *ICube Laboratory, University of Strasbourg, 300 Bd Sebastien Brant, Illkirch, 67412, France*
[b] *INSA Strasbourg, 24 Bd de la Victoire, Strasbourg, 67000, France*

Abstract

In this article, thrusters embedded on a cable-driven parallel robot (CDPR) platform are proposed to improve the CDPR dynamics and trajectory tracking performance. On-board thrusters with their short response time can compensate for the reduced bandwidth of the winch actuation due to winding speed limit and low cable stiffness. To compute and allocate control signals to winches and thrusters, a nonlinear model predictive controller (NMPC) is designed. A model of a CDPR with its hybrid actuation dynamics and saturation is introduced, including an alternative model of the thrust actuation that removes the need of thrust sensors and reduces the size of the NMPC optimization problem. To achieve a zero steady-state error with the NMPC, which becomes offset-free, an augmented model including additional disturbance states is proposed. The theoretical conditions to achieve offset-free control are checked. The proposed NMPC scheme is validated experimentally on a planar CDPR with three cables and four propeller-based thrusters. Results show that onboard thrusters contribute to a tracking error reduction along complex trajectories and an efficient damping of the platform vibration.

Keywords: Cable-driven parallel robot, Propeller-based thruster, Cable elasticity, Control allocation, Model Predictive Control

Notation

The following notations are used: scalar values are written with a normal font, lowercase (λ, n,...), vectors with a bold font, lowercase ($\boldsymbol{x}$, $\mathbf{f}$, ...) and matrices with a bold font, uppercase ($\mathbf{M}$, $\mathbf{W_f}$,...). The projection of a vector $\mathbf{v}$ in a reference frame $\mathcal{F}_g$ is denoted by ${}^g\mathbf{v}$.

The symbols $\mathbb{I}_n$ and $\mathbf{0}_{m\times n}$ represent the identity matrix and a null matrix of dimension ($n\times n$) and ($m\times n$) respectively. The notation $\mathbf{M}^+$ is used for the Moore–Penrose inverse of a non-square matrix $\mathbf{M}$. The notations diag($\mathbf{v}$) and blkdiag($\mathbf{A}$, $\mathbf{B}$, $\mathbf{C}$) denote a diagonal matrix with the entries of vector $\mathbf{v}$ on its diagonal and a block diagonal matrix composed of the matrices $\mathbf{A}$, $\mathbf{B}$, and $\mathbf{C}$ on its diagonal, respectively.

*Corresponding author
Email addresses: l.cuvillon@unistra.fr (Loïc Cuvillon), marpaperozo@unistra.fr (Miguel Arpa Perozo), ardayigit4@gmail.com (Arda Yiğit), sylvain.durand@insa-strasbourg.fr (Sylvain Durand), jacques.gangloff@unistra.fr (Jacques Gangloff)

1. Introduction

Cable-driven parallel robots (CDPRs) have received a growing interest since the beginning of the century. They have been proposed for numerous applications [1]: heavy load manipulation, rehabilitation, 3D printing, radio-telescope antenna positioning,...

One specificity of CDPRs is that the rigid linkages of common parallel robots are replaced by cables. Using cables, CDPRs can achieve a high payload to robot mass ratio, large workspace, high-speed motion and cost effectiveness. However, the drawbacks inherent to cables are unilateral force –a cable can only pull and not push– and elasticity.

To cope with the unilateral force of cables, redundant antagonist cables are used to ensure the existence of a sufficient large wrench feasible workspace, which is the space where a set of wrenches (force and moment) can be applied on the platform without violating the tension limits of the cables [2]. In the case of suspended CDPRs, where all cables are above the platform, the gravity acts as an antagonist cable of constant direction. Be-

sides, a tension distribution or tension allocation algorithm has to be implemented to ensure the positive tension of all the cables during the motion [3, 4].

The cable elasticity impairs the CDPR dynamics and performance. The settling time of the platform is increased due to its low stiffness, resulting in low damped and low frequency oscillation modes of the platform [5, 6]. In addition, the force bandwidth of the cable actuation [7] is limited by the winch speed saturation: according to Hooke's law, the higher the cable elasticity (i.e. the lower the stiffness), the longer the length of cable to wind for a desired force on the platform. These performance issues are especially relevant for applications involving very long cables related to a large workspace, or applications using synthetic ropes of low weight and low stiffness. Some examples of such CDPR applications are facade cleaning [8], facade construction [9] or sports event broadcasting with an on-board camera (CableCam, SkyCam [10]).

Several approaches have been proposed to reject the low-damped vibration of the platform. The first proposition has been to increase the platform stiffness by increasing its antagonist stiffness part, i.e. increasing the tension of antagonist cables without modifying the wrench exerted on the platform [5]. However, this approach may yield in high tensions for some cable configurations and is simply inapplicable to suspended CDPRs which have no antagonist cables in the vertical direction. Winch torque control [11, 12] and winch position control [6, 8, 13] have been proposed for active vibration compensation. However, the efficiency and robustness of these approaches may be limited by the reduced force bandwidth of the winch, as mentioned earlier, and by the non-collocated way of controlling the CDPR platform [14]: the measurement of the vibration on the platform and actuation through the winches are separated by an elastic transmission.

Therefore, embedding additional actuators on the platform has been proposed to further improve vibration rejection. Inertia-based actuators have been proposed with reaction wheels [15], pendulum or balancing arms [16, 17, 18]. However, inertia-based actuators are usually bulky, they modify the platform inertia when active, and they can only exert a transient wrench on the platform until they reach their maximum velocity or maximum motion range.

To overcome some of these limitations, cold gas or propeller-based thrusters have been lastly proposed as embedded actuators. They can generate a permanent wrench, have short response time and do not modify the platform inertia when active. Cold-gas thrusters [19] and propeller-based thrusters from unmanned aerial vehicles (UAV) [20, 21, 22] have already been evaluated and have proved their efficiency to actively damp the vibration of CDPR platforms.

Association of cable winch and thruster has been proposed for other purposes than vibration dampening. Earlier in [23], a thruster has been used on a facade-cleaning planar robot to generate a constant out-of-plane force with the aim to keep adhesion of the robot to the wall. More recently, suspended aerial manipulators have been introduced in [21, 24]. The aerial manipulator is suspended by one cable to a crane or flying carrier in order to compensate for the gravity and to coarsely position the aerial manipulator. Actuated rigging cables are used to regulate the position of the platform center of gravity during the motion of an on-board industrial manipulator. Lastly, a concept similar to an aerial CDPR has been developed in [25], where UAVs carry the cable winches and act as movable anchoring points for the cables.

However, the concept of Hybrid Cable-Thruster actuated (HCT-actuated) system seems to have been first introduced in [26]. In this work, cable actuation is added to an underwater vehicle working under a vessel or an offshore platform. The aim is to increase the wrench feasible workspace with the combined action of cables and thrusters, such that heavier loads can be lifted and a steadier pose achieved. More recently, propeller-based thrusters have been considered in [27] with the same objective of extending the workspace and increasing the payload of CDPRs. The arrangement of the thrusters on the CDPR platform is optimized in order to deliver a desired set of wrenches over the whole workspace.

The works mentioned above have considered additional thrusters either to improve vibration rejection or to increase the CDPR workspace in a quasi-static scenario. Except for our preliminary work [22], none has yet explicitly tackled the simultaneous control of actuators with different bandwidths to improve the performance of a CDPR pose trajectory tracking. The fast response of the thrusters and their additional wrench could improve the tracking of high-speed trajectories with sudden change of direction. In particular, high-bandwidth thrusters can compensate for the low-bandwidth winches when using long or elastic cables. For suspended CDPR, the thrusters could increase the downward acceleration to overcome the limit of gravity.

To exploit the over-actuated hybrid cable-thruster system, an optimal distribution of the control signals between the actuators is required. The different band-

widths of the actuator dynamics and their different saturation limits have to be taken into account. This distribution problem is known as control allocation. Control allocation [28] has been studied in the past for aircraft, spacecraft, water surface, underwater or electric vehicles.

Among the techniques to solve the control allocation problem (see the survey paper [28]), model predictive control (MPC) allocation has been evaluated [29, 30]. MPC uses a model of the system dynamics to predict its temporal behavior on a horizon and explicitly takes into account constraints on the system states and input control signals. Thus, the determination of the control wrench and its allocation to the actuators can be handled simultaneously within the MPC constrained optimization. In [29], model predictive control allocation is applied to the guidance of a re-entry vehicle. Actuator dynamics of the vehicle are modeled as a second-order system in the MPC prediction model. The tracking accuracy of the vehicle attitude is improved compared to a classic static allocation that neglects the actuator dynamics.

MPC has been applied with success to CDPRs in order to control the platform pose and solve the tension distribution problem [17, 31, 32]. In [32], a nonlinear model predictive control (NMPC) is designed based on the nonlinear equations of motion of a CDPR with cable-only actuation. A dynamically computed tension target is introduced in the NMPC cost function to solve the tension distribution problem and minimize the norm of the cable tensions. However, like in other predictive controls of CDPRs, the actuator dynamics are not considered.

In our previous work [22], a CDPR with redundant actuation using high-bandwidth propeller-based thrusters was studied. It was experimentally demonstrated that thrusters can improve the tracking of step trajectories and the rejection of disturbances. The CDPR was a simple 2 degrees-of-freedom (DoF) robot suspended by one elastic cable. Based on a linearized model of this CDPR, a linear MPC was designed but its validity was restricted to the vicinity of an operating point.

In this paper, a NMPC is proposed to extend the control over the whole workspace of a CDPR with n DoFs, taking into account the CDPR nonlinear dynamics and the dynamics of the hybrid actuators. Particularly, the NMPC is tailored for CDPRs whose cable elasticity cannot be neglected. While this elasticity impairs the platform dynamics and stiffness, there is a benefit: the cable tension can be finely monitored through the cable elongation and the tension can be controlled with a position or velocity controlled winch [13]. Thus, a CDPR with a hybrid thruster and velocity-controlled winch actuation is considered in this work.

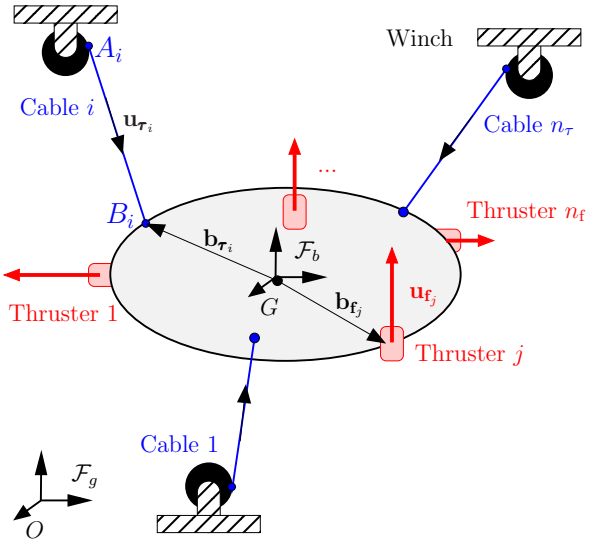

Fig. 1: Cable-driven parallel robot with n_τ cables and n_f on-board thrusters.

The NMPC objective is to improve the CDPR dynamics and trajectory tracking performance. Moreover, to ensure zero steady-state error, an offset-free NMPC formulation is proposed based on a model of the system augmented with constant disturbances [33]. The sufficient condition on the system, the controller and the state observer to achieve a zero steady-state error are verified for the proposed NMPC. The control law is assessed experimentally on a 3-DoF planar suspended CDPR with three cables and four propellers.

The remainder of the paper is organized as follows. Section II describes the system and dynamic equations of a CDPR with on-board actuators. Section III introduces the predictive control strategy with offset-free steady state. The robot prototype and the experimental results are presented in Section IV. Section V concludes the paper.

2. System Modeling

A CDPR with n_τ cables and n_f on-board thrusters is considered (Fig. 1). Thrusters can be mounted on the platform for various reasons depending on the application. For example, it is possible to substitute a thruster for a cable in order to remove a winch or avoid interference between the cables as proposed in [27]. It is also

possible to complement the cables instead of replacing them. The objective is to improve the damping of the platform vibration and improve the tracking of trajectories as studied in this paper. To control the n DoFs of a CDPR with hybrid actuation, the design constraint is $n_\tau + n_\mathrm{f} \geq n$. Moreover, if a static pose of the CDPR platform has to be maintained with only the cables, the additional design constraint on the number of cables is $n_\tau \geq n$ for a suspended CDPR or $n_\tau \geq n+1$ for a fully-constrained CDPR [5].

2.1. Platform Dynamics

Let $\boldsymbol{x} = [\mathbf{p}(t)^\mathrm{T}, \boldsymbol{\theta}(t)^\mathrm{T}]^\mathrm{T} \in \mathbb{R}^n$ be the pose of the CDPR platform with respect to an inertial reference frame $\mathcal{F}_g$. The vector $\mathbf{p}$ gives the coordinates of the platform center of gravity G. The vector $\boldsymbol{\theta}$ is a vector of Euler angles describing its orientation, i.e. the rotation between $\mathcal{F}_g$ and a frame $\mathcal{F}_b$ of origin G attached to the platform body.

The vectors of cable tensions $\boldsymbol{\tau}$ and thruster forces (or thrusts) $\mathbf{f}$ model the forces acting on the platform. Based on the Newton-Euler formulation [13, 32], the equation of the platform motion is (cable mass is neglected):

$$\begin{bmatrix} m\,\mathbb{I} & \mathbf{0} \\ \mathbf{0} & \mathbf{I_g} \end{bmatrix} \begin{bmatrix} \ddot{\mathbf{p}} \\ \dot{\boldsymbol{\omega}} \end{bmatrix} + \begin{bmatrix} \mathbf{0} \\ \boldsymbol{\omega} \times \mathbf{I_g}\boldsymbol{\omega} \end{bmatrix} + \begin{bmatrix} -m\mathbf{g} \\ \mathbf{0} \end{bmatrix} = \mathbf{W}_{\boldsymbol{\tau}}\,\boldsymbol{\tau} + \mathbf{W}_\mathbf{f}\,\mathbf{f} \quad (1)$$

with $\boldsymbol{\omega}$ the angular velocity of the platform with respect to the frame $\mathcal{F}_g$, $\mathbf{g}$ the gravity vector, m the platform mass and $\mathbf{I_g}(\boldsymbol{x})$ its inertia matrix expressed in the inertial frame.

The matrices $\mathbf{W}_{\boldsymbol{\tau}}$ and $\mathbf{W}_\mathbf{f}$ are wrench matrices mapping the cable tensions $\boldsymbol{\tau}$ and the thrusts $\mathbf{f}$ to the resulting wrenches exerted on the platform. The wrench matrix $\mathbf{W}_{\boldsymbol{\tau}} \in \mathbb{R}^{n \times n_\tau}$ maps the cable tensions $\boldsymbol{\tau}$ to the force $\mathbf{F}_{\boldsymbol{\tau}}$ and moment $\mathbf{N}_{\boldsymbol{\tau}}$ applied to the platform:

$$\begin{bmatrix} {}^g\mathbf{F}_{\boldsymbol{\tau}} \\ {}^g\mathbf{N}_{\boldsymbol{\tau}} \end{bmatrix} = \mathbf{W}_{\boldsymbol{\tau}}(\boldsymbol{x})\,\boldsymbol{\tau} \quad (2)$$

$$= -\begin{bmatrix} {}^g\mathbf{u}_{\boldsymbol{\tau}_1} & \dots & {}^g\mathbf{u}_{\boldsymbol{\tau}_{n_\tau}} \\ {}^g\mathbf{b}_{\boldsymbol{\tau}_1} \times^g \mathbf{u}_{\boldsymbol{\tau}_1} & \dots & {}^g\mathbf{b}_{\boldsymbol{\tau}_{n_\tau}} \times^g \mathbf{u}_{\boldsymbol{\tau}_{n_\tau}} \end{bmatrix} \boldsymbol{\tau} \quad (3)$$

with ${}^g\mathbf{u}_{\boldsymbol{\tau}_i}(\boldsymbol{x})$, the i^th cable unit direction vector, and ${}^g\mathbf{b}_{\boldsymbol{\tau}_i}(\boldsymbol{x})$, the position of the cable attachment point B_i expressed in $\mathcal{F}_g$ (see Fig. 1). The rotation matrix between $\mathcal{F}_g$ and $\mathcal{F}_b$ is denoted by $\mathbf{R}_{gb}$. The vector ${}^g\mathbf{u}_{\boldsymbol{\tau}_i}(\boldsymbol{x})$ is defined by $\frac{{}^g\mathbf{b}_{\boldsymbol{\tau}_i}(\boldsymbol{x}) - {}^g\mathbf{a}_{\boldsymbol{\tau}_i}}{\|\mathbf{b}_{\boldsymbol{\tau}_i} - \mathbf{a}_{\boldsymbol{\tau}_i}\|_2}$ with ${}^g\mathbf{a}_{\boldsymbol{\tau}_i}$, the position of the winch cable output A_i and ${}^g\mathbf{b}_{\boldsymbol{\tau}_i}(\boldsymbol{x}) = \mathbf{p} + \mathbf{R}_{gb}(\boldsymbol{\theta})\,{}^b\mathbf{b}_{\boldsymbol{\tau}_i}$.

Similarly to the cable actuation, the resulting wrench $\mathbf{w_f}$ from the thruster forces on the platform is given by:

$${}^b\mathbf{w_f} = \begin{bmatrix} {}^b\mathbf{F_f} \\ {}^b\mathbf{N_f} \end{bmatrix} = \begin{bmatrix} {}^b\mathbf{u}_{\mathbf{f}_1} & \dots & {}^b\mathbf{u}_{\mathbf{f}_{n_\mathrm{f}}} \\ {}^b\mathbf{b}_{\mathbf{f}_1} \times^b \mathbf{u}_{\mathbf{f}_1} & \dots & {}^b\mathbf{b}_{\mathbf{f}_{n_\mathrm{f}}} \times^b \mathbf{u}_{\mathbf{f}_{n_\mathrm{f}}} \end{bmatrix} \mathbf{f} \quad (4)$$

$$= {}^b\mathbf{W_f}\,\mathbf{f} \quad (5)$$

where ${}^b\mathbf{u}_{\mathbf{f}_j}$ is the thrust direction, ${}^b\mathbf{b}_{\mathbf{f}_j}$ the thruster position (see Fig. 1) and ${}^b\mathbf{W_f}$ the resulting configuration matrix, all expressed in the platform body frame $\mathcal{F}_b$. If propeller-based thrusters are used, the motor torque and gyroscopic torque due to the spinning of the propeller can be added to $\mathbf{w_f}$ or neglected considering them as unmodeled disturbances. Since non-orientable thrusters are considered, ${}^b\mathbf{W_f}$ is constant when expressed in $\mathcal{F}_b$. Projecting the resulting wrench $\mathbf{w_f}$ in the inertial frame $\mathcal{F}_g$ yields the wrench matrix $\mathbf{W_f} \in \mathbb{R}^{n \times n_\mathrm{f}}$:

$${}^g\mathbf{w_f} = \mathbf{W_f}(\boldsymbol{\theta})\,\mathbf{f} \quad (6)$$

$$\text{with } \mathbf{W_f}(\boldsymbol{\theta}) = \begin{bmatrix} \mathbf{R}_{gb}(\boldsymbol{\theta}) & \mathbf{0} \\ \mathbf{0} & \mathbf{R}_{gb}(\boldsymbol{\theta}) \end{bmatrix} {}^b\mathbf{W_f} \quad (7)$$

Let $\mathbf{S}(\boldsymbol{\theta})$ be the matrix that maps the time derivative of the Euler angles $\boldsymbol{\theta}$ to the angular velocity $\boldsymbol{\omega}$ (see Analytical Jacobian definition in [34]), such that $\boldsymbol{\omega} = \mathbf{S}(\boldsymbol{\theta})\dot{\boldsymbol{\theta}}$. By substituting this expression of $\boldsymbol{\omega}$ in (1), the CDPR model in the Cartesian/task space becomes:

$$\mathbf{M}(\boldsymbol{x})\ddot{\boldsymbol{x}} + \mathbf{C}(\boldsymbol{x}, \dot{\boldsymbol{x}})\dot{\boldsymbol{x}} + \mathbf{G_g} = \begin{bmatrix} \mathbf{W}_{\boldsymbol{\tau}}(\boldsymbol{x}) & \mathbf{W_f}(\boldsymbol{\theta}) \end{bmatrix} \begin{bmatrix} \boldsymbol{\tau} \\ \mathbf{f} \end{bmatrix} \quad (8)$$

where the inertia matrix $\mathbf{M}$, the Coriolis and centrifugal wrench matrix $\mathbf{C}$, the gravity force $\mathbf{G_g}$ are given by:

$$\mathbf{M}(\boldsymbol{x}) = \begin{bmatrix} m\mathbb{I} & \mathbf{0} \\ \mathbf{0} & \mathbf{I_g}\mathbf{S} \end{bmatrix}, \quad \mathbf{G_g} = \begin{bmatrix} -m\mathbf{g} \\ \mathbf{0} \end{bmatrix} \quad (9a)$$

$$\mathbf{C}(\boldsymbol{x}, \dot{\boldsymbol{x}})\dot{\boldsymbol{x}} = \begin{bmatrix} \mathbf{0} \\ \mathbf{I_g}\dot{\mathbf{S}}\dot{\boldsymbol{\theta}} + \mathbf{S}\,\dot{\boldsymbol{\theta}} \times \mathbf{I_g}\mathbf{S}\,\dot{\boldsymbol{\theta}} \end{bmatrix} \quad (9b)$$

2.2. Thruster Dynamics

To enhance the dynamic behavior of the CDPR, n_f additional thrusters are embedded in the platform. Cold-gas thrusters or air propellers could be used among others. The thruster is selected such that its thrust bandwidth is larger than the force bandwidth of the cable actuation. The thrust limits are modeled as input saturation with $\mathrm{f_{min}} \leq \mathrm{f}^* \leq \mathrm{f_{max}}$, where f^* is the thruster force control input. In the case of a unidirectional thruster, the lower bound on the thrust becomes $\mathrm{f_{min}} = 0\,\mathrm{N}$ instead of $\mathrm{f_{min}} = -\mathrm{f_{max}}$.

A transfer function of the thrust dynamics can be obtained through the identification process of one thruster

on a test bench. Consider $G_{\mathrm{f}}(s)$ the minimal realization of the transfer function between the control signal f^* and output f:

$$G_{\mathrm{f}}(s) = \frac{\mathrm{f}(s)}{\mathrm{f}^*(s)} = \frac{b_{m_{\mathrm{f}}-1} s^{m_{\mathrm{f}}-1} + \cdots + b_1 s + b_0}{s^{m_{\mathrm{f}}} + \cdots + a_1 s + a_0} \tag{10}$$

with m_{f}, the order of the transfer function, and s, the Laplace variable. It is assumed that all the poles are distinct and stable, and $b_0 \neq 0$ such that the static gain is finite and non-zero. A model of the thruster dynamics in the time domain can be derived from the coefficients of the polynomial fraction $G_{\mathrm{f}}(s)$ in the form of a state-space representation [35]. The state-space model of the thruster dynamics is a differential equation of the following form:

$$\dot{\mathbf{x}}_{\mathrm{f}} = \mathbf{A}_{\mathrm{f}}\, \mathbf{x}_{\mathrm{f}} + \mathbf{b}_{\mathrm{f}}\, \mathrm{f}^* \tag{11}$$

$$\mathrm{f} = \mathbf{c}_{\mathrm{f}}^{\mathrm{T}}\, \mathbf{x}_{\mathrm{f}} \tag{12}$$

with $\mathbf{x}_{\mathrm{f}} \in \mathbf{R}^{m_{\mathrm{f}}}$, the state vector which uniquely defines the system state at instant t; $\mathbf{A}_{\mathrm{f}}$, the state matrix describing the unforced evolution of the system over time; $\mathbf{b}_{\mathrm{f}}$, the input matrix describing the influence of the input on the system state; and $\mathbf{c}_{\mathrm{f}}^{\mathrm{T}}$, the output matrix providing the system output.

Let $\mathbf{f} = [\mathrm{f}_1, \ldots, \mathrm{f}_{n_{\mathrm{f}}}]^{\mathrm{T}}$ be the thrust vector of the n_{f} identical and independent thrusters. Then, the wrench $\mathbf{w_f}$ (6) exerted by the thrusters on the platform is governed by the state-space model (Fig. 2a):

$$\dot{\mathbf{x}}_{\mathbf{f}} = \mathbf{A_f}\, \mathbf{x_f} + \mathbf{B_f}\, \mathbf{f}^* \tag{13}$$

$$\mathbf{w_f} = \mathbf{W_f}(\boldsymbol{\theta})\, \mathbf{C_f}\, \mathbf{x_f} \tag{14}$$

$$\mathbf{f}_{\min} \leq \mathbf{f}^* \leq \mathbf{f}_{\max} \quad \text{(input constraints)} \tag{15}$$

with $\mathbf{x_f} \in \mathbb{R}^{n_{\mathrm{f}} m_f}$ the thruster actuation state vector, and the following expressions of the matrices :

$$\mathbf{A_f} = \mathrm{blkdiag}(\mathbf{A}_{\mathrm{f}}, \ldots, \mathbf{A}_{\mathrm{f}}) \quad \in \mathbb{R}^{n_{\mathrm{f}} m_{\mathrm{f}} \times n_{\mathrm{f}} m_{\mathrm{f}}} \tag{16}$$

$$\mathbf{B_f} = \mathrm{blkdiag}(\mathbf{b}_{\mathrm{f}}, \ldots, \mathbf{b}_{\mathrm{f}}) \quad \in \mathbb{R}^{n_{\mathrm{f}} m_{\mathrm{f}} \times n_{\mathrm{f}}} \tag{17}$$

$$\mathbf{C_f} = \mathrm{blkdiag}(\mathbf{c}_{\mathrm{f}}^{\mathrm{T}}, \ldots, \mathbf{c}_{\mathrm{f}}^{\mathrm{T}}) \quad \in \mathbb{R}^{n_{\mathrm{f}} \times n_{\mathrm{f}} m_{\mathrm{f}}} \tag{18}$$

For some geometric configuration of the thrusters and notably all the configurations with a redundant number of thrusters $n_{\mathrm{f}} > n$, the wrench matrix $\mathbf{W_f} \in \mathbb{R}^{n \times n_{\mathrm{f}}}$ is not full column rank. If the wrench matrix $\mathbf{W_f}$ is not full column rank, then a linearized model of the Hybrid CDPR around a steady state is not observable without the measurement of the thrusts $\mathbf{f}$. Indeed, since the dimension of the nullspace of $\mathbf{W_f}$ is not zero, there exist

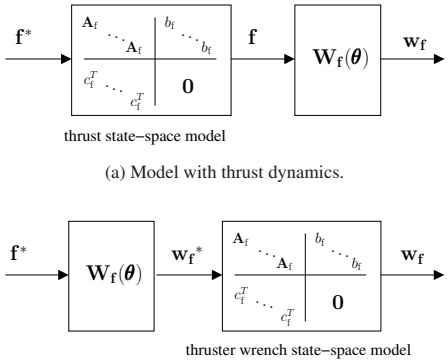

(a) Model with thrust dynamics.

(b) Alternative model with wrench dynamics.

Fig. 2: Alternatives for the thruster actuation model.

infinitely many thrust vectors $\mathbf{f}$ (i.e. states $\mathbf{x_f}$) that match a wrench $\underline{\mathbf{w}}_{\mathbf{f}}$ observed on the platform:

$$\mathbf{f} = \mathbf{W}_{\mathbf{f}}^{+}\, \underline{\mathbf{w}}_{\mathbf{f}} + \mathbf{f_{null}} \tag{19}$$

with $\mathbf{f_{null}}$, any thrust vector in Null($\mathbf{W_f}$), the nullspace of $\mathbf{W_f}$ defined by $\mathbf{W_f}\, \mathbf{f_{null}} = \mathbf{0}$.

However, the measurement of $\mathbf{f}$ requires to embed thrust sensors on the platform. Besides, adding these measurements to the CDPR model will increase the number of state variables in the NMPC offset-free problem. Increasing the number of states results in increasing the computational time to solve the NMPC optimization problem.

To overcome these issues, an alternative model of the thruster actuation is proposed (Fig. 2b):

$$\dot{\mathbf{x}}_{\mathbf{w_f}} = \mathbf{A_f}\, \mathbf{x}_{\mathbf{w_f}} + \mathbf{B_f}\, \mathbf{W_f}(\boldsymbol{\theta})\, \mathbf{f}^* \tag{20}$$

$$\mathbf{w_f} = \mathbf{C_f}\, \mathbf{x}_{\mathbf{w_f}} \tag{21}$$

$$\mathbf{f}_{\min} \leq \mathbf{f}^* \leq \mathbf{f}_{\max} \quad \text{(input constraints)} \tag{22}$$

with $\mathbf{x}_{\mathbf{w_f}} \in \mathbb{R}^{n\, m_{\mathrm{f}}}$ the wrench state vector, and the following redefinition of the matrix dimensions:

$$\mathbf{A_f} = \mathrm{blkdiag}(\mathbf{A}_{\mathrm{f}}, \ldots, \mathbf{A}_{\mathrm{f}}) \quad \in \mathbb{R}^{n\, m_{\mathrm{f}} \times n\, m_{\mathrm{f}}} \tag{23}$$

$$\mathbf{B_f} = \mathrm{blkdiag}(\mathbf{b}_{\mathrm{f}}, \ldots, \mathbf{b}_{\mathrm{f}}) \quad \in \mathbb{R}^{n\, m_{\mathrm{f}} \times n} \tag{24}$$

$$\mathbf{C_f} = \mathrm{blkdiag}(\mathbf{c}_{\mathrm{f}}^{\mathrm{T}}, \ldots, \mathbf{c}_{\mathrm{f}}^{\mathrm{T}}) \quad \in \mathbb{R}^{n \times n\, m_{\mathrm{f}}} \tag{25}$$

Providing that all the actuators have the same linear dynamics, this actuation model is derived from (13)-(14) through a change of state variables (see Appendix A). While the previous model (13)-(14) uses state variables describing thrust dynamics, the alternative model uses state variables describing the wrench dynamics. This alternative model is observable from the wrench $\mathbf{w_f}$ ex-

erted on the platform without requiring additional measurements. Since a minimal representation of the transfer function G_f is observable [35], the pair $\{\mathbf{A}_\mathrm{f}, \mathbf{c}_\mathrm{f}^\mathrm{T}\}$ is observable. Thus the pair $\{\mathbf{A_f}, \mathbf{C_f}\}$ of the alternative model is observable, independently of the column rank of $\mathbf{W_f}$.

Considering the exact state-space model (A.6) that describes the wrench dynamics, its state-space matrix is a function of the thruster dynamics ($-\frac{1}{T_\mathrm{f}}\mathbb{I}_n = \mathbf{A_f}$ in (A.6)) and a function of the angular velocity $\boldsymbol{\omega}$ of the platform. In this model, the wrench resulting from the thrust references $\mathbf{f}^*$ is first projected into the inertial frame with $\mathbf{W_f}(\boldsymbol{\theta}(t))$ (7). As a consequence, during the settling time of the wrench, the wrench direction is modified. This effect is taken into account in the wrench dynamics (A.6) with its dependence on $\boldsymbol{\omega}$.

Thereby, the proposed alternative model (20)-(21) neglects the effect of the platform rotation. The alternative model is exact only if $\boldsymbol{\omega} = 0$ during the settling of the thrust, i.e. if the platform orientation remains constant. If $\boldsymbol{\omega} \neq 0$, based on the equation (A.6), the alternative model is still a good approximation of the wrench dynamics if:

$$\forall i, \quad \|\boldsymbol{\omega}\|_2 \ll \left\| \frac{1}{T_{\mathrm{f}_i}} \right\|_2 \tag{26}$$

with $T_{\mathrm{f}_i} = -\frac{1}{\lambda_{\mathrm{f}_i}}$, the time constant associated with the eigenvalue λ_{f_i} of $\mathbf{A}_\mathrm{f}$ (or equivalently the pole λ_{f_i} of G_f). In other words, the alternative model is valid if the settling time of the thruster is short enough with respect to the angular velocity, such that the rotation of the platform during the settling of the thrust $\mathbf{f}$ is negligible. If the condition (26) does not hold, the model (13)-(14) can be used despite its drawbacks, or the exact model of the wrench dynamics (A.6) can be used assuming that a measurement of $\boldsymbol{\omega}$ is available.

2.3. Winch Actuator Dynamics

If the cable stiffness is low due to its length or material, the cable tension can be measured and controlled through the cable elongation [36, 13]. In this context, a cable is modeled as a linear spring with a negligible mass. Under tension, its straight length between its attachment points A_i and B_i (see Fig. 1) is its geometric length $\mathrm{l}_{1_i}(\boldsymbol{x}) = \|{}^g\mathbf{b}_{\boldsymbol{\tau}_i}(\boldsymbol{x}) - {}^g\mathbf{a}_{\boldsymbol{\tau}_i}\|_2$. The cable unstretched length, i.e. the cable length when its tension is zero, is denoted l_{2_i}.

The axial stiffness of the cable i is $k_{a_i} = ea/l_{2_i}$, where e is the Young modulus of the cable and a its cross-sectional area as in [11, 14]. Let $\mathbf{l_2} = [l_{2_1}, \ldots, l_{2_{n_\tau}}]^\mathrm{T}$ be the vector of the n_τ unstretched lengths of the cables. Then, the vector of the cable tensions $\boldsymbol{\tau} \in \mathbb{R}^{n_\tau}$ is given by:

$$\boldsymbol{\tau} = \mathbf{K_a}(\mathbf{l_2})\,[\mathbf{l_1}(\boldsymbol{x}) - \mathbf{l_2}] \tag{27}$$

$$\mathbf{0} < \boldsymbol{\tau}(\boldsymbol{x}, \mathbf{l_2}) \leq \boldsymbol{\tau}_\mathbf{max} \text{ (algebraic constraints)} \tag{28}$$

with $\mathbf{K_a} = \mathrm{diag}(k_{a_1}, \ldots, k_{a_{n_\tau}})$, the diagonal matrix of the cable stiffness and $(\mathbf{l_1} - \mathbf{l_2})$ the vector of cable elongations. As the cables can only pull and not push, the positivity constraint on each tension $0 \leq \tau_i$ translates into the constraint (28), where $\boldsymbol{\tau}_\mathrm{max} = [\tau_{\mathrm{max}_1}, \ldots, \tau_{\mathrm{max}_{n_\tau}}]^\mathrm{T}$ is the upper-bound vector of the admissible tensions.

The cable tensions $\boldsymbol{\tau}$ are controlled by modifying the cable unstretched lengths $\mathbf{l_2}$, also called free lengths, with the winches. Assuming that the tension of the cable stored in the winch spool is zero, the cable lengths $\mathbf{l_2}$ are linked to the angular positions $\boldsymbol{\alpha}$ of the winch motors by $\mathbf{l_2} = r\,\boldsymbol{\alpha}$ where r is the radius of the winch spool.

The control input of the winch motor drive is assumed to be a velocity reference, i.e. a winding velocity reference $\dot{l}_2^*$. If the inner loop gains of the motor controller are high, the dynamics of the winch can be considered decoupled from the platform dynamics [13]. However, the actuator performance is limited by its maximum cable winding velocity $\dot{l}_{2\,\mathrm{max}}$. Similarly to the thruster dynamic model (10), consider a minimal transfer function $G_{l_2}(s)$ identified on a winch between the winding velocity reference $\dot{l}_2^*$ and cable length l_2:

$$\begin{aligned} G_{l_2}(s) = \frac{l_2(s)}{\dot{l}_2^*(s)} &= \frac{b_{m_\tau-1}s^{m_\tau-1} + \cdots + b_1 s + b_0}{s^{m_\tau} + \cdots + a_1 s + a_0} \cdot \frac{1}{s} \\ &= G_{\dot{l}_2}(s) \cdot \frac{1}{s} \end{aligned} \tag{29}$$

with the same assumption on $G_{\dot{l}_2}(s)$ as on $G_\mathrm{f}(s)$. Let $\left\{\mathbf{A}_{l_2}, \mathbf{b}_{l_2}, \mathbf{c}_{l_2}^\mathrm{T}\right\}$ be the state, input and output matrices of a state-space representation of $G_{\dot{l}_2}(s)$, the velocity dynamics of the winch. The state vector of this representation is denoted by $\mathbf{x}_{l_2} \in \mathbf{R}^{m_\tau}$.

A state-space representation of the n_τ winch actuators dynamics is given by:

$$\dot{\mathbf{x}}_{\mathbf{l_2}} = \begin{bmatrix} \mathbf{0} & \mathbf{0} \\ \mathbf{B}_{\mathbf{l_2}} & \mathbf{A}_{\mathbf{l_2}} \end{bmatrix} \mathbf{x}_{\mathbf{l_2}} + \begin{bmatrix} \mathbb{I} \\ \mathbf{0} \end{bmatrix} \dot{\mathbf{l}}_\mathbf{2}^* \tag{30}$$

$$\mathbf{l_2} = \begin{bmatrix} \mathbf{0} & \mathbf{C}_{\mathbf{l_2}} \end{bmatrix} \mathbf{x}_{\mathbf{l_2}} \tag{31}$$

$$-\dot{\mathbf{l}}_{\mathbf{2}\mathrm{max}} \leq \dot{\mathbf{l}}_\mathbf{2}^* \leq \dot{\mathbf{l}}_{\mathbf{2}\mathrm{max}} \text{ (input constraints)} \tag{32}$$

with $\dot{\mathbf{l}}_\mathbf{2}^* = [\dot{l}_{2_1}^*, \ldots, \dot{l}_{2_{n_\tau}}^*]^\mathrm{T}$ the winding velocity control

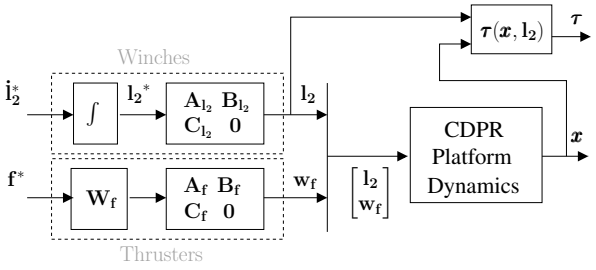

Fig. 3: Model of CDPR with its hybrid cable-thruster actuation dynamics.

inputs, and the matrices:

$$\mathbf{A_{l_2}} = \text{blkdiag}(\mathbf{A}_{l_2}, \ldots, \mathbf{A}_{l_2}) \quad \mathbf{A_{l_2}} \in \mathbb{R}^{n_\tau m_\tau \times n_\tau m_\tau} \tag{33}$$

$$\mathbf{B_{l_2}} = \text{blkdiag}(\mathbf{b}_{l_2}, \ldots, \mathbf{b}_{l_2}) \tag{34}$$

$$\mathbf{C_{l_2}} = \text{blkdiag}(\mathbf{c}_{l_2}^{\mathrm{T}}, \ldots, \mathbf{c}_{l_2}^{\mathrm{T}}) \tag{35}$$

The cable actuation state vector is $\mathbf{x_{l_2}} = [\mathbf{l_2^{*\mathrm{T}}}\ \mathbf{x_{i_2}}^{\mathrm{T}}]^{\mathrm{T}} \in \mathbb{R}^{n_\tau(m_\tau+1)}$, where $\mathbf{l_2^*} = [l_{2_1}^*, \ldots, l_{2_{n_\tau}}^*]^{\mathrm{T}}$ is the integral of the control input $\mathbf{\dot{l}_2^*}$. For clarity of presentation, the integration of the velocity signal is considered at the input of the actuation model instead of the output as visible in the winch actuation block of Fig. 3. This reverse order does not modify the input-output behavior of the winch actuation model.

2.4. CDPR with Hybrid Actuation Dynamics

The full model is obtained by connecting the actuation models (20) and (30) to the CDPR platform model (8), as presented in Fig. 3. The state vector of the hybrid actuation is denoted by $\mathbf{x_u} = [\mathbf{x_{l_2}}^{\mathrm{T}}\ \mathbf{x_{w_f}}^{\mathrm{T}}]^{\mathrm{T}}$, and its state-space matrices by:

$$\mathbf{A_u} = \left[\begin{array}{cc:c} \mathbf{0} & \mathbf{0} & \mathbf{0} \\ \mathbf{B_{l_2}} & \mathbf{A_{l_2}} & \mathbf{0} \\ \hdashline \mathbf{0} & \mathbf{0} & \mathbf{A_f} \end{array}\right], \ \mathbf{B_u} = \left[\begin{array}{c:c} \mathbb{I} & \mathbf{0} \\ \mathbf{0} & \mathbf{0} \\ \hdashline \mathbf{0} & \mathbf{B_f}\,\mathbf{W_f}(\boldsymbol{\theta}) \end{array}\right] \tag{36}$$

It yields the following nonlinear model of the CDPR:

$$\begin{bmatrix} \ddot{\boldsymbol{x}} \\ \dot{\boldsymbol{x}} \\ \dot{\mathbf{x}}_\mathbf{u} \end{bmatrix} = \begin{bmatrix} \boldsymbol{\phi}(\dot{\boldsymbol{x}}, \boldsymbol{x}, \mathbf{x_u}) \\ \dot{\boldsymbol{x}} \\ \mathbf{A_u x_u} \end{bmatrix} + \begin{bmatrix} \mathbf{0} \\ \mathbf{0} \\ \mathbf{B_u} \end{bmatrix} \mathbf{u} \tag{37}$$

$$\text{s.t.} \begin{bmatrix} -\mathbf{\dot{l}_{2max}} \\ \mathbf{f_{min}} \end{bmatrix} \leq \mathbf{u} \leq \begin{bmatrix} \mathbf{\dot{l}_{2max}} \\ \mathbf{f_{max}} \end{bmatrix} \qquad \text{(input constraint)} \tag{38}$$

$$\mathbf{0} \leq \boldsymbol{\tau}(\boldsymbol{x}, \mathbf{l_2}) \leq \boldsymbol{\tau}_{\mathbf{max}} \qquad \text{(algebraic constraint)} \tag{39}$$

with $\mathbf{u} = [\mathbf{\dot{l}_2^{*\mathrm{T}}}\ \mathbf{f}^{*\mathrm{T}}]^{\mathrm{T}}$, the control input, and $\boldsymbol{\phi}$, the function:

$$\begin{aligned} \boldsymbol{\phi}(\dot{\boldsymbol{x}}, \boldsymbol{x}, \mathbf{x_u}) = &(\mathbf{M}(\boldsymbol{x}))^{-1} \Big[-\mathbf{C}(\boldsymbol{x}, \dot{\boldsymbol{x}})\dot{\boldsymbol{x}} - \mathbf{G_g} \\ &+ [\mathbf{W}_{\boldsymbol{\tau}}(\boldsymbol{x}) \quad \mathbb{I}_n] \begin{bmatrix} \mathbf{K_a}[\mathbf{l_1}(\boldsymbol{x}) - \mathbf{C_{l_2}} \mathbf{x_{i_2}}] \\ \mathbf{C_f x_{w_f}} \end{bmatrix} \Big] \end{aligned} \tag{40}$$

The system output $\mathbf{y} \in \mathbb{R}^{n_y}$ is composed of the pose of the platform $\boldsymbol{x}$ and the cable tensions $\boldsymbol{\tau}$, such that:

$$\mathbf{y} = \begin{bmatrix} \boldsymbol{x} \\ \boldsymbol{\tau} \end{bmatrix} = \boldsymbol{g}(\mathbf{x}) = \begin{bmatrix} \boldsymbol{x} \\ \mathbf{K_a}(\mathbf{C_{l_2}} \mathbf{x_{i_2}})[\mathbf{l_1}(\boldsymbol{x}) - \mathbf{C_{l_2}} \mathbf{x_{i_2}}] \end{bmatrix} \tag{41}$$

where $\mathbf{x} = [\dot{\boldsymbol{x}}^{\mathrm{T}}\ \boldsymbol{x}^{\mathrm{T}}\ \mathbf{x_{l_2}}^{\mathrm{T}}\ \mathbf{x_{w_f}}^{\mathrm{T}}]^{\mathrm{T}} \in \mathbb{R}^{n_x}$ is the state vector of the CDPR with its hybrid actuator dynamics.

3. Control

Efficient control of the pose of the hybrid CDPR requires to solve the control allocation problem to cope with the different force bandwidths and constraints of the two actuation systems. Model predictive control (MPC) can intrinsically take into account constraints and has been successfully used to solve redundancy or control allocation problem [30, 22, 32]. Moreover, if a preview of the reference trajectory is available, MPC control signals can anticipate the reference changes to further improve the tracking accuracy.

3.1. Prediction Model and Augmented Model

Based on a prediction model of the system output, the MPC selects the sequence of control signal samples that minimizes an objective function on a finite time horizon.

Since, in general, no discrete-time closed-form model can be derived from a nonlinear continuous-time model, a numerical integration of the differential equation is used to predict the system output at the sampling instants. A discrete-time model of the system dynamics can be derived using a Runge-Kutta (RK) integration method. For the sake of simplicity, a low order Euler integration method is considered for the prediction model as in [32]:

$$\mathbf{x}(t_k + \Delta t) = \mathbf{x}(t_k) + \Delta t\ \dot{\mathbf{x}}(t_k, \mathbf{u}(t_k)) \tag{42}$$

where Δt is the sampling period, $t_k = k\,\Delta t$, $k \in \mathbb{N}$, and $\dot{\mathbf{x}}(t_k, \mathbf{u}(t_k))$ is provided by the system dynamics model.

A state-space representation of the CDPR with a hybrid actuation is given by:

$$\dot{\mathbf{x}} = \boldsymbol{f}(\mathbf{x}) + \mathbf{F_u}(\mathbf{x})\,\mathbf{u} \tag{43}$$

$$\mathbf{y} = \boldsymbol{g}(\mathbf{x}) \tag{44}$$

where $\boldsymbol{f}$ and $\mathbf{F_u}$ are the appropriate functions defined by model (37). Using Euler integration, a discrete-time state-space model of the system is:

$$\mathbf{x}_{k+1} = \mathbf{x}_k + \Delta t \left[\boldsymbol{f}(\mathbf{x}_k) + \mathbf{F_u}(\mathbf{x}_k)\,\mathbf{u}_k\right] \tag{45}$$

$$\mathbf{y}_k = \boldsymbol{g}(\mathbf{x}_k) \tag{46}$$

To achieve an offset-free MPC, i.e. with no steady-state error, the requirements are (section 4.2.6 in [37]):

- the minimum of the cost function must correspond to zero tracking error;
- the prediction must be unbiased at steady state, i.e. the output $\mathbf{y}_k$ of the model has to match the output $\mathbf{y}_{\mathbf{m}_k}$ measured on the system.

A relevant approach for unbiased prediction and thus for offset-free control is to augment the model with a disturbance model [33, 38]. Constant disturbances are introduced in the model to capture any output bias due to model uncertainties or external disturbances. The vector of the disturbances, $\mathbf{d}$, is then estimated simultaneously with the system state $\mathbf{x}$ by a state observer. Under certain conditions [33] verified in Section 3.4, the estimate $\hat{\mathbf{d}}_k$ converges towards a steady state and ensures there is no mismatch between the model output $\mathbf{y}_k$ and the measured plant output $\mathbf{y}_{\mathbf{m}_k}$.

Therefore, the following augmented model is proposed as the prediction model of the offset-free NMPC:

$$\begin{aligned}\mathbf{x}_{k+1} &= \boldsymbol{f}_{\mathbf{aug}}(\mathbf{x}_k, \mathbf{d}_k, \mathbf{u}_k)\\ &= \mathbf{x}_k + \Delta t \left[\boldsymbol{f}(\mathbf{x}_k) + \mathbf{F_u}(\mathbf{x}_k)\,\mathbf{u}_k + \mathbf{F_d}(\mathbf{x}_k)\,\mathbf{d}_k\right]\end{aligned} \tag{47}$$

$$\mathbf{d}_{k+1} = \mathbf{d}_k \tag{48}$$

$$\mathbf{y}_k = \boldsymbol{g}(\mathbf{x}_k) \tag{49}$$

where $\boldsymbol{f}_{\mathbf{aug}}$ is the augmented state function and $\mathbf{F_d}(\mathbf{x}_k) = [(\mathbf{M}^{-1}(\boldsymbol{x}))^{\mathrm{T}}\,\mathbf{0}^{\mathrm{T}}]^{\mathrm{T}}$ such that the disturbance $\mathbf{d}_k \in \mathbb{R}^n$ is equivalent to a wrench disturbance on the CDPR platform.

3.2. Offset-free NMPC

Thrusters are embedded on the CDPR platform to improve the tracking performance of a pose trajectory $\boldsymbol{x}_{\mathbf{r}}$. To reduce energy consumption and noise level of the thrusters, it is desirable that the thrusters are off ($\mathbf{f} = \mathbf{0}$) at steady state. Thus, the following definition of the static workspace [39] is given:

Definition 1. The static workspace $\mathbb{W}$ of the CDPR is defined by the set of the poses $\bar{\boldsymbol{x}}$, where $\mathbf{W}_{\boldsymbol{\tau}} \in \mathbb{R}^{n\times n_\tau}$ is full row rank and $\bar{\boldsymbol{x}}$ is a static pose of the platform that can be maintained using exclusively the cable tensions.

A consequence of this definition is that the number n_τ of cables has to be equal to or greater than the number of DoFs: $n_\tau \geq n$.

The NMPC is achieved by solving an optimal control problem (OCP) to determine the first sample $\mathbf{u}_0$ of a control signal sequence $[\mathbf{u}_0, \ldots, \mathbf{u}_{N-1}]$ that minimizes an objective function on a receding time horizon of N samples. The OCP is solved at each sample time k and its solution $\mathbf{u}_0^*$ is applied to the system, such that $\mathbf{u}_k = \mathbf{u}_0^*$.

To track the reference trajectory $\boldsymbol{x}_{\mathbf{r}_k}$, the OCP to solve at each sample time k is:

$$\begin{aligned}\underset{\mathbf{u}_0,\ldots,\mathbf{u}_{N-1}}{\text{minimize}} \quad & \sum_{j=0}^{N-1} \left\|\mathbf{y}_j - \mathbf{y}_{\mathbf{r}_j}\right\|^2_{\mathbf{Q_y}} + \left\|\mathbf{u}_j\right\|^2_{\mathbf{Q_u}}\\ \text{subject to} \quad & \mathbf{x}_{j+1} = \boldsymbol{f}_{\mathbf{aug}}(\mathbf{x}_j, \mathbf{d}_0, \mathbf{u}_j),\\ & \mathbf{y}_j = \boldsymbol{g}(\mathbf{x}_j),\\ & \mathbf{x}_0 = \hat{\mathbf{x}}_k,\ \mathbf{d}_0 = \hat{\mathbf{d}}_k,\\ & \mathbf{h_l} \leq \mathbf{h}(\mathbf{x}_j, \mathbf{u}_j) \leq \mathbf{h_h}\end{aligned} \tag{50}$$

where $\mathbf{y}_{\mathbf{r}\,j} = [\boldsymbol{x}_{\mathbf{r}_{k+j}}^T\ \bar{\boldsymbol{\tau}}_k^{\mathrm{T}}]^{\mathrm{T}}$ is the reference for the system output $\mathbf{y}_j$, and $\bar{\boldsymbol{\tau}}_k$ is a target for the cable tensions at steady state. The function $\boldsymbol{f}_{\mathbf{aug}}$ in the OCP is the nonlinear augmented model (47) of the CDPR plant. To initialize the problem, the vectors $\mathbf{x_0}$ and $\mathbf{d_0}$ are set to $\hat{\mathbf{x}}_k$ and $\hat{\mathbf{d}}_k$, the current estimates of the state and constant disturbance. The operator $\|\cdot\|_{\mathbf{P}}$ is defined such that $\|\mathbf{v}\|^2_{\mathbf{P}} = \mathbf{v}^{\mathrm{T}}\mathbf{P}\mathbf{v}$, and the weighting matrices are $\mathbf{Q_y} > \mathbf{0}$ and $\mathbf{Q_u} > \mathbf{0}$, positive definite. The output weights are tuned such that the pose trajectory tracking is a primary objective, while the steady-state tension distribution is a secondary objective.

The constraints (39) on the cable tensions and (38) on the actuator inputs are gathered into one constraint function:

$$\mathbf{h}(\mathbf{x}_j, \mathbf{u}_j) = \left[\boldsymbol{\tau}(\boldsymbol{x}_j, \mathbf{l_2}_j)^{\mathrm{T}} \quad \dot{\mathbf{l}}_{\mathbf{2}_j}^{*\,\mathrm{T}} \quad \mathbf{f}_j^{*\mathrm{T}}\right]^{\mathrm{T}} \tag{51}$$

with the following lower and upper bounds:

$$\mathbf{h_l} = \left[\mathbf{0}_{n_\tau\times 1}{}^{\mathrm{T}} \quad -\dot{\mathbf{l}}_{\mathbf{2max}}{}^{T} \quad \mathbf{f_{min}}{}^{T}\right]^{\mathrm{T}} \tag{52}$$

$$\mathbf{h_h} = \left[\boldsymbol{\tau}_{\mathbf{max}}{}^{\mathrm{T}} \quad \dot{\mathbf{l}}_{\mathbf{2max}}{}^{T} \quad \mathbf{f_{max}}{}^{T}\right]^{\mathrm{T}} \tag{53}$$

These constraints ensure that the cable tensions and the control inputs of the actuators are admissible along the trajectory.

If the cables are redundant ($n_\tau > n$), multiple tension distributions $\boldsymbol{\tau}$ or equivalently cable lengths $\mathbf{l_2}$ are consistent with a given pose trajectory. Thus, the target $\bar{\boldsymbol{\tau}}$ in the OCP cost function allows for selecting a particular cable tension distribution when the trajectory reaches a

steady-state pose $\bar{\boldsymbol{x}}$.

3.3. Tension Target at Steady State

For a desired steady-state pose $\boldsymbol{x}_{\mathbf{r}_k} = \bar{\boldsymbol{x}}$, let us define the corresponding targets $\bar{\boldsymbol{\tau}}_k$ for the cable tensions and $\bar{\mathbf{u}}_k$ for the control signals. These targets are solutions of the equilibrium system:

$$\bar{\mathbf{x}}_k = \boldsymbol{f}_{\mathbf{aug}}(\bar{\mathbf{x}}_k, \hat{\mathbf{d}}_k, \bar{\mathbf{u}}_k) \tag{54}$$

$$\bar{\mathbf{y}}_k = \begin{bmatrix} \bar{\boldsymbol{x}} \\ \bar{\boldsymbol{\tau}}_k \end{bmatrix} = \boldsymbol{g}(\bar{\mathbf{x}}_k) \tag{55}$$

with $\bar{\mathbf{x}}_k$, the state vector at steady state.

For any steady-state pose $\bar{\boldsymbol{x}} \in \mathbb{W}$, an optimal control target is $\bar{\mathbf{u}} = [\bar{\mathbf{i}}_2^{*\mathrm{T}}\ \bar{\mathbf{f}}^{*\mathrm{T}}]^{\mathrm{T}} = \mathbf{0}$:

- the steady-state condition (54) with definition (47) of $\boldsymbol{f}_{\mathbf{aug}}$ enforces $\bar{\mathbf{i}}_2^* = \mathbf{0}$;
- $\bar{\mathbf{f}}^* = \mathbf{0}$ is an admissible solution from Definition 1 that minimizes the thrust at steady state.

Solving the system (54)-(55) for $\bar{\mathbf{u}} = \mathbf{0}$ yields the kineto-static equation:

$$\mathbf{G}_{\mathbf{g}} - \hat{\mathbf{d}}_k = \mathbf{W}_{\boldsymbol{\tau}}(\boldsymbol{x}_{\mathbf{r}_k})\, \mathbf{K}_{\mathbf{a}}(\bar{\mathbf{l}}_{2_k}) \left[\mathbf{l}_1(\boldsymbol{x}_{\mathbf{r}_k}) - \bar{\mathbf{l}}_{2_k}\right] \tag{56}$$

$$= \mathbf{W}_{\boldsymbol{\tau}}(\boldsymbol{x}_{\mathbf{r}_k})\, \bar{\boldsymbol{\tau}}_k \tag{57}$$

with the expression of $\boldsymbol{\tau}$ given by (27).

The tension $\bar{\boldsymbol{\tau}}_k$, solution of this equation, is given by:

$$\begin{aligned} \bar{\boldsymbol{\tau}}_k &= \bar{\boldsymbol{\tau}}_{\mathbf{d}_k} + \boldsymbol{\tau}_{\mathbf{Null}} \\ &= \bar{\boldsymbol{\tau}}_{\mathbf{d}_k} + \mathbf{N}_{\boldsymbol{\tau}}(\boldsymbol{x}_{\mathbf{r}_k})\, \boldsymbol{\eta} \end{aligned} \tag{58}$$

with $\bar{\boldsymbol{\tau}}_{\mathbf{d}_k} = (\mathbf{W}_{\boldsymbol{\tau}}(\boldsymbol{x}_{\mathbf{r}_k}))^{+}[\mathbf{G}_{\mathbf{g}} - \hat{\mathbf{d}}_k]$ and $\boldsymbol{\tau}_{\mathbf{Null}} \in \mathrm{Null}(\mathbf{W}_{\boldsymbol{\tau}})$, any vector in the nullspace of the cable wrench matrix.

Let $r = n_\tau - n$ be the degree of redundancy of the cable actuation. The columns of matrix $\mathbf{N}_{\boldsymbol{\tau}} \in \mathbb{R}^{n_\tau \times r}$ form an orthonormal basis of $\mathrm{Null}(\mathbf{W}_{\boldsymbol{\tau}})$, such that $\mathbf{N}_{\boldsymbol{\tau}}^{\mathrm{T}}\mathbf{N}_{\boldsymbol{\tau}} = \mathbb{I}_r$. Thereby, $\boldsymbol{\tau}_{\mathbf{Null}} = \mathbf{N}_{\boldsymbol{\tau}}\boldsymbol{\eta}$, where $\boldsymbol{\eta}$ is an arbitrary vector of dimension r, is a tension vector belonging to $\mathrm{Null}(\mathbf{W}_{\boldsymbol{\tau}})$. The vector $\bar{\boldsymbol{\tau}}_{\mathbf{d}_k}$ is the minimal-norm solution of $\mathbf{W}_{\boldsymbol{\tau}}(\boldsymbol{x}_{\mathbf{r}_k})\,\bar{\boldsymbol{\tau}}_k = \mathbf{G}_{\mathbf{g}} - \hat{\mathbf{d}}_k$, which verifies $\mathbf{N}_{\boldsymbol{\tau}}^{\mathrm{T}}\,\bar{\boldsymbol{\tau}}_{\mathbf{d}_k} = \mathbf{0}$ [3].

To minimize energy consumption at steady state, various optimization algorithms [4, 3] can be used to search for a vector $\boldsymbol{\eta}$ that minimizes a norm of the tension vector $\|\bar{\boldsymbol{\tau}}_k\|$ under the constraint of positive tensions. This tension optimization problem is solved at each time step to update the target $\bar{\boldsymbol{\tau}}_k$ in the OCP (50) cost function.

If the cables are not redundant ($n_\tau = n$), $\mathbf{W}_{\boldsymbol{\tau}}$ is square and full rank on $\mathbb{W}$ and only one tension $\boldsymbol{\tau}$ matches the wrench exerted on the platform. Thus, if the cables are not redundant, the tension target can be removed from the OCP problem. The reference and control variables are then redefined by: $\mathbf{y}_{\mathbf{r}\,j} = \boldsymbol{x}_{\mathbf{r}k+j}$ and $\mathbf{y}_j = \boldsymbol{x}_j$.

The OCP problem can be implemented and solved with the `acados` framework [40], which proposes a Runge-Kutta RK4 integration method of the continuous-time nonlinear CDPR dynamics. Considering an exteroceptive sensor to measure the pose $\boldsymbol{x}_k$ and an extended Kalman filter (EKF) to observe the CDPR states and disturbances, a block diagram of the NMPC control is presented in Fig. 4.

3.4. Conditions for Offset-free Control

A MPC is said to be offset-free if its steady-state tracking error converges to zero. In this section, the offset-free conditions are verified for the NMPC described by (50). The proof of offset-free tracking is based on the theorem in [33]. The theorem states that the number n_{dist} of constant disturbances in the augmented model has to be equal to the number n_y of measurements ($n_{dist} = n_y$) [33, 38].

The cable actuation model (30) with the control signal $\dot{\mathbf{l}}_2^*$ as input and the state $\mathbf{l}_2 \in \mathbb{R}^{n_\tau}$ as output (Fig. 3) contains a number n_τ of integrators. These integrators behave as an input disturbance model when coupled with a state observer: the input signal integration and the mismatches between plant and model are combined by the observer in an estimate $\hat{\mathbf{l}}_2^*$ of the integrator outputs (see the δu-formulation section in [38]). In addition, a number n of disturbances have been explicitly introduced in the CDPR augmented model (47)-(49) through the wrench disturbance vector $\mathbf{d} \in \mathbb{R}^n$, such that the total number of disturbances is $n_{dist} = n_\tau + n$. As the number of measurements is $n_y = n + n_\tau$, with $\mathbf{y} = [\boldsymbol{x}^{\mathrm{T}}\,\boldsymbol{\tau}^{\mathrm{T}}]^{\mathrm{T}}$, the initial assumption $n_{dist} = n_y$ is verified.

In the case of non-redundant cables ($n_\tau = n$), the system output is just $\mathbf{y} = \boldsymbol{x}$ and thus $n_y = n = n_\tau$. With the n_τ disturbances lumped into the estimates $\hat{\mathbf{l}}_2^*$ of the cable free length, the initial assumption $n_{dist} = n_\tau = n_y$ is verified. Thereby, the model (45)-(46) is used in this case without the addition of a disturbance $\mathbf{d}$.

The other assumptions that need to be tested for an offset-free control are [33]:

1) Observability . For any admissible $(\mathbf{y}^*, \mathbf{u}^*)$, there exist a unique $(\mathbf{x}, \mathbf{d})$ such that:

$$\mathbf{x} = \boldsymbol{f}_{\mathbf{aug}}(\mathbf{x}, \mathbf{d}, \mathbf{u}^*) \tag{59}$$

$$\mathbf{y}^* = \boldsymbol{g}(\mathbf{x}) \tag{60}$$

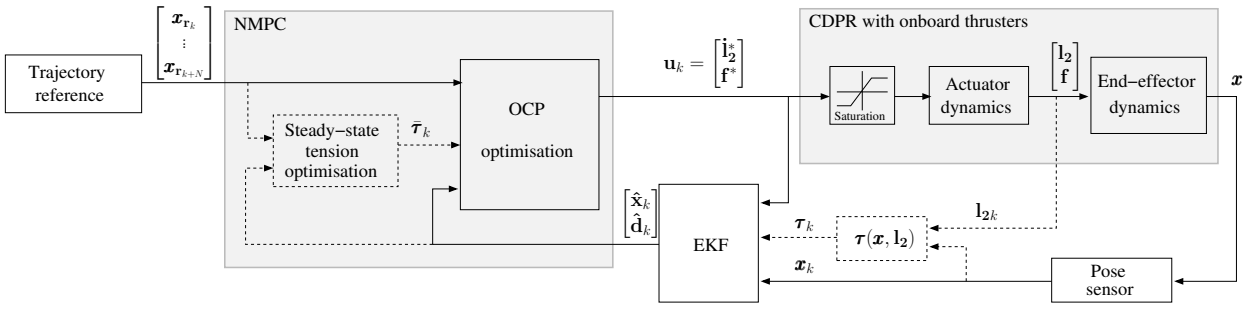

Fig. 4: NMPC scheme for CDPRs with on-board thrusters. The block in dotted lines are removed from the scheme if the cables are not redundant ($n_\tau = n$).

This assumption ensures that the disturbance model has been adequately chosen, i.e. that any system output $\mathbf{y}$ for a given $\mathbf{u}$ can be the outcome of a specific disturbance $\mathbf{d}$ on the system. This assumption can be tested with Theorem 2 in [33]. Based on the implicit function theorem, this theorem converts the unique solution of (59)-(60) condition into a rank condition on a matrix of the functions $\boldsymbol{f}_{\mathbf{aug}}$ and $\boldsymbol{g}$ Jacobians. With $\mathbf{d} \in \mathbb{R}^n$ and the remaining n_τ disturbances included in the state $\mathbf{l}_2^*$ of vector $\mathbf{x}$, the rank condition to verify is:

$$\operatorname{rank}\begin{bmatrix}\mathbf{F_x} - \mathbb{I}_{n_\mathrm{x}} & \mathbf{F_d} \\ \mathbf{G_x} & \mathbf{G_d}\end{bmatrix} = n_\mathrm{x} + n \tag{61}$$

with the Jacobians, evaluated at a steady state $(\bar{\mathbf{x}}, \bar{\mathbf{u}}, \bar{\mathbf{d}})$:

$$\frac{\partial}{\partial \mathbf{x}} \boldsymbol{f}_{\mathbf{aug}}(\bar{\mathbf{x}}, \bar{\mathbf{u}}, \bar{\mathbf{d}}) = \mathbf{F_x}, \qquad \frac{\partial}{\partial \mathbf{d}} \boldsymbol{f}_{\mathbf{aug}}(\bar{\mathbf{x}}, \bar{\mathbf{u}}, \bar{\mathbf{d}}) = \mathbf{F_d} \tag{62}$$

$$\frac{\partial}{\partial \mathbf{x}} \boldsymbol{g}(\bar{\mathbf{x}}) = \mathbf{G_x}, \qquad \frac{\partial}{\partial \mathbf{d}} \boldsymbol{g}(\bar{\mathbf{x}}) = \mathbf{G_d} = \mathbf{0} \tag{63}$$

Based on the linearized model (B.11)-(B.12) of the augmented system derived in Appendix B, the matrix of condition (61) becomes (with $\Delta t = 1$):

$$\left[\begin{array}{cccccc} \mathbf{0} & -\mathbf{M}^{-1}\mathbf{K}_{\boldsymbol{x}} & \mathbf{0} & \mathbf{M}^{-1}\mathbf{W}_{\boldsymbol{\tau}}\mathbf{T}_{\mathbf{l}_2}\mathbf{C}_{\mathbf{l}_2} & \mathbf{M}^{-1}\mathbf{C_f} & \mathbf{M}^{-1} \\ \mathbb{I}_n & \mathbf{0} & \mathbf{0} & \mathbf{0} & \mathbf{0} & \mathbf{0} \\ \mathbf{0} & \mathbf{0} & \mathbf{0} & \mathbf{0} & \mathbf{0} & \mathbf{0} \\ \mathbf{0} & \mathbf{0} & \mathbf{B}_{\mathbf{l}_2} & \mathbf{A}_{\mathbf{l}_2} & \mathbf{0} & \mathbf{0} \\ \mathbf{0} & \mathbf{0} & \mathbf{0} & \mathbf{0} & \mathbf{A_f} & \mathbf{0} \\ \hdashline \mathbf{0} & \mathbb{I}_n & \mathbf{0} & \mathbf{0} & \mathbf{0} & \mathbf{0} \\ \mathbf{0} & \mathbf{T}_{\boldsymbol{x}} & \mathbf{0} & \mathbf{T}_{\mathbf{l}_2}\mathbf{C}_{\mathbf{l}_2} & \mathbf{0} & \mathbf{0} \end{array}\right] \tag{64}$$

Omitting the line of null matrices irrelevant for the rank, the matrix can be transformed through row and column exchanges in the upper triangular block matrix:

$$\begin{bmatrix} \mathbb{I}_n & \mathbf{0} & \mathbf{0} & \mathbf{0} & \mathbf{0} & \mathbf{0} \\ \mathbf{0} & \mathbf{M}^{-1} & \mathbf{M}^{-1}\mathbf{W}_{\boldsymbol{\tau}}\mathbf{T}_{\mathbf{l}_2}\mathbf{C}_{\mathbf{l}_2} & \mathbf{0} & \mathbf{M}^{-1}\mathbf{C_f} & -\mathbf{M}^{-1}\mathbf{K}_{\boldsymbol{x}} \\ \mathbf{0} & \mathbf{0} & \mathbf{A}_{\mathbf{l}_2} & \mathbf{B}_{\mathbf{l}_2} & \mathbf{0} & \mathbf{0} \\ \mathbf{0} & \mathbf{0} & \mathbf{T}_{\mathbf{l}_2}\mathbf{C}_{\mathbf{l}_2} & \mathbf{0} & \mathbf{0} & \mathbf{T}_{\boldsymbol{x}} \\ \mathbf{0} & \mathbf{0} & \mathbf{0} & \mathbf{0} & \mathbf{A_f} & \mathbf{0} \\ \mathbf{0} & \mathbf{0} & \mathbf{0} & \mathbf{0} & \mathbf{0} & \mathbb{I}_n \end{bmatrix} \tag{65}$$

The square matrix (65) is full rank, if the matrix $\mathbf{A_f}$ and the following block matrix on its diagonal are full rank:

$$\begin{bmatrix} \mathbf{A}_{\mathbf{l}_2} & \mathbf{B}_{\mathbf{l}_2} \\ \mathbf{T}_{\mathbf{l}_2}\mathbf{C}_{\mathbf{l}_2} & \mathbf{0} \end{bmatrix} = \begin{bmatrix} \mathbb{I}_{n_\tau m_\tau} & \mathbf{0} \\ \mathbf{0} & \mathbf{T}_{\mathbf{l}_2} \end{bmatrix} \begin{bmatrix} \mathbf{A}_{\mathbf{l}_2} & \mathbf{B}_{\mathbf{l}_2} \\ \mathbf{C}_{\mathbf{l}_2} & \mathbf{0} \end{bmatrix} \tag{66}$$

Since $G_\mathrm{f}(s)$ (Section 2.2) is supposed to have only stable poles, there is no zero eigenvalue; thus matrix $\mathbf{A_f}$ is full rank. Since $\mathbf{T}_{\mathbf{l}_2} \in \mathbb{R}^{n_\tau \times n_\tau}$ is full rank from expression (B.5), the block matrix is full rank if the right matrix in the product (66) is full rank. According to the definition (33) of $\mathbf{A}_{\mathbf{l}_2}$, $\mathbf{B}_{\mathbf{l}_2}$ and $\mathbf{C}_{\mathbf{l}_2}$, elementary column and row exchanges show that:

$$\operatorname{rank}\begin{bmatrix} \mathbf{A}_{\mathbf{l}_2} & \mathbf{B}_{\mathbf{l}_2} \\ \mathbf{C}_{\mathbf{l}_2} & \mathbf{0} \end{bmatrix} = n_\tau . \operatorname{rank}\begin{bmatrix} \mathbf{A}_{l_2} & \mathbf{b}_{l_2} \\ \mathbf{c}_{l_2}^{\mathrm{T}} & 0 \end{bmatrix} \tag{67}$$

Assuming that $\mathbf{A}_{l_2}$, $\mathbf{b}_{l_2}$ and $\mathbf{c}_{l_2}$ are in an observable canonical form [35], it yields through elementary column exchanges:

$$\operatorname{rank}\begin{bmatrix} \mathbf{A}_{l_2} & \mathbf{b}_{l_2} \\ \mathbf{c}_{l_2}^{\mathrm{T}} & 0 \end{bmatrix} = \operatorname{rank}\begin{bmatrix} 1 \ldots 0 & 0 & b_{m_{l_2}} & -a_{m_{l_2}} \\ \vdots \ldots \vdots & \vdots & \vdots & \vdots \\ 0 \ldots 0 & 1 & b_1 & -a_1 \\ 0 \ldots 0 & 0 & b_0 & -a_0 \\ 0 \ldots 0 & 0 & 0 & 1 \end{bmatrix} \tag{68}$$

The triangular matrix in (68) is full rank, since $b_0 \neq 0$ from the assumption that $G_{j_2}(s)$ has a non-zero gain

(Section 2.3). Thereby, the matrix (65) is full column rank and the observability assumption holds.

2) Controllability. The vector $\bar{\mathbf{y}} = [\bar{\boldsymbol{x}}^{\mathrm{T}}\ \bar{\boldsymbol{\tau}}(\bar{\mathbf{x}})^{\mathrm{T}}]^{\mathrm{T}}$ represents a pose and a corresponding tension among all the admissible tensions at steady state. However, $\bar{\mathbf{y}}$ is not an unconstrained, nor a minimal representation: the vector $\bar{\boldsymbol{\tau}}$ has to verify to the kineto-static equation (56), while all the admissible $\bar{\boldsymbol{\tau}} \in \mathbb{R}^{n_\tau}$ can be described uniquely by the pose $\bar{\boldsymbol{x}}$ and the free parameter $\boldsymbol{\eta} \in \mathbb{R}^r$ ($r \leq n_\tau$) based on (58).

For a well-posed definition of the controllability assumption, let us define the minimal representation $\mathbf{y_c} = [\boldsymbol{x}^{\mathrm{T}}\ \boldsymbol{\eta}^{\mathrm{T}}]^{\mathrm{T}} \in \mathbb{R}^{n_{\mathrm{yc}}}$ of the controlled variables $\mathbf{y} = [\boldsymbol{x}^{\mathrm{T}}\ \boldsymbol{\tau}^{\mathrm{T}}]^{\mathrm{T}}$, where $\boldsymbol{\eta}$ is the parameter characterizing a steady-state tension distribution among all the admissible distributions. From properties of the unique decomposition (58) of the tension vector $\boldsymbol{\tau}$, the output $\boldsymbol{\eta}$ is obtained from:

$$\boldsymbol{\eta} = \mathbf{N}_{\boldsymbol{\tau}}^{\mathrm{T}}(\boldsymbol{x})\ \boldsymbol{\tau}(\mathbf{x}) \tag{69}$$

Controllability assumption. For all $(\mathbf{y}_\mathbf{c}^*, \mathbf{d}^*)$, there exist a unique $(\mathbf{x}, \mathbf{u})$ with $\mathbf{u} = [\dot{\mathbf{l}}_2^{*\mathrm{T}}\ \mathbf{0}^{\mathrm{T}}]^{\mathrm{T}}$ such that:

$$\mathbf{x} = \boldsymbol{f}_{\mathbf{aug}}(\mathbf{x}, \mathbf{u}, \mathbf{d}^*) \tag{70}$$

$$\mathbf{y}_\mathbf{c}^* = \begin{bmatrix} \boldsymbol{x}^* \\ \boldsymbol{\eta}^* \end{bmatrix} = \begin{bmatrix} \boldsymbol{x}^* \\ \mathbf{N}_{\boldsymbol{\tau}}^{\mathrm{T}}\ \boldsymbol{\tau}(\mathbf{x}) \end{bmatrix} \tag{71}$$

This controllability assumption ensures the existence of a control signal $\mathbf{u}$ and state $\mathbf{x}$ compatible with the steady-state output $\mathbf{y}_c^* = [\boldsymbol{x}^{*\mathrm{T}}\boldsymbol{\eta}^{*\mathrm{T}}]^{\mathrm{T}}$, for any constant disturbance $\mathbf{d}^*$. The controllability is assessed for the restrictive case where only the cable actuation ($\mathbf{f}^* = \mathbf{0}$) is used to maintain the steady state, as explained in Section 3.2.

Similarly to the observability, the controllability condition can be converted into a rank condition using Theorem 3 in [33]. This yields the condition:

$$\operatorname{rank} \begin{bmatrix} \mathbf{F}_\mathbf{x} - \mathbb{I}_{n_\mathrm{x}} & \mathbf{F}_{\dot{\mathbf{l}}_2^*} \\ \mathbf{G}_{\mathbf{c}_\mathbf{x}} & \mathbf{0} \end{bmatrix} = n_\mathrm{x} + n_\tau \tag{72}$$

with the Jacobians:

$$\mathbf{F}_{\dot{\mathbf{l}}_2^*} = \frac{\partial}{\partial \dot{\mathbf{l}}_2^*} \boldsymbol{f}_{\mathbf{aug}}(\bar{\mathbf{x}}, \bar{\mathbf{u}}, \bar{\mathbf{d}}), \quad \mathbf{G}_{\mathbf{c}_\mathbf{x}} = \frac{\partial}{\partial \mathbf{x}} \begin{bmatrix} \bar{\boldsymbol{x}} \\ \mathbf{N}_{\boldsymbol{\tau}}^{\mathrm{T}}(\bar{\boldsymbol{x}})\ \boldsymbol{\tau}(\bar{\mathbf{x}}) \end{bmatrix} \tag{73}$$

Based on the linearized model (B.11)-(B.12) of the augmented system, the matrix in (72) becomes:

$$\left[\begin{array}{cccccc} \mathbf{0} & -\mathbf{M}^{-1}\mathbf{K}_{\boldsymbol{x}} & \mathbf{0} & \mathbf{M}^{-1}\mathbf{W}_{\boldsymbol{\tau}}\mathbf{T}_{\mathbf{l}_2}\mathbf{C}_{\mathbf{l}_2} & \mathbf{M}^{-1}\mathbf{C}_\mathbf{f} & \mathbf{0} \\ \mathbb{I}_n & \mathbf{0} & \mathbf{0} & \mathbf{0} & \mathbf{0} & \mathbf{0} \\ \mathbf{0} & \mathbf{0} & \mathbf{0} & \mathbf{0} & \mathbf{0} & \mathbb{I}_{n_\tau} \\ \mathbf{0} & \mathbf{0} & \mathbf{B}_{\mathbf{l}_2} & \mathbf{A}_{\mathbf{l}_2} & \mathbf{0} & \mathbf{0} \\ \mathbf{0} & \mathbf{0} & \mathbf{0} & \mathbf{0} & \mathbf{A}_\mathbf{f} & \mathbf{0} \\ \hdashline \mathbf{0} & \mathbb{I}_n & \mathbf{0} & \mathbf{0} & \mathbf{0} & \mathbf{0} \\ \mathbf{0} & \mathbf{N}_{\boldsymbol{x}} & \mathbf{0} & \mathbf{N}_{\boldsymbol{\tau}}^{\mathrm{T}}\mathbf{T}_{\mathbf{l}_2}\mathbf{C}_{\mathbf{l}_2} & \mathbf{0} & \mathbf{0} \end{array}\right] \tag{74}$$

where $\mathbf{N}_{\boldsymbol{x}}(\bar{\boldsymbol{x}}, \bar{\mathbf{l}}_\mathbf{2}) = \frac{\partial}{\partial \boldsymbol{x}}\boldsymbol{\eta}(\bar{\mathbf{x}})$.

Column and row exchanges yield the following upper triangular block matrix:

$$\left[\begin{array}{cccccc} \mathbb{I}_{n_\tau} & \mathbf{0} & \mathbf{0} & \mathbf{0} & \mathbf{0} & \mathbf{0} \\ \mathbf{0} & \mathbb{I}_n & \mathbf{0} & \mathbf{0} & \mathbf{0} & \mathbf{0} \\ \mathbf{0} & \mathbf{0} & \mathbf{A}_{\mathbf{l}_2} & \mathbf{B}_{\mathbf{l}_2} & \mathbf{0} & \mathbf{0} \\ \mathbf{0} & \mathbf{0} & \mathbf{M}^{-1}\mathbf{W}_{\boldsymbol{\tau}}\mathbf{T}_{\mathbf{l}_2}\mathbf{C}_{\mathbf{l}_2} & \mathbf{0} & \mathbf{M}^{-1}\mathbf{C}_\mathbf{f} & -\mathbf{M}^{-1}\mathbf{K}_{\boldsymbol{x}} \\ \mathbf{0} & \mathbf{0} & \mathbf{N}_{\boldsymbol{\tau}}^{\mathrm{T}}\mathbf{T}_{\mathbf{l}_2}\mathbf{C}_{\mathbf{l}_2} & \mathbf{0} & \mathbf{0} & \mathbf{N}_{\boldsymbol{x}} \\ \mathbf{0} & \mathbf{0} & \mathbf{0} & \mathbf{0} & \mathbf{A}_\mathbf{f} & \mathbf{0} \\ \mathbf{0} & \mathbf{0} & \mathbf{0} & \mathbf{0} & \mathbf{0} & \mathbb{I}_n \end{array}\right] \tag{75}$$

This matrix is full rank if the following block matrix on the diagonal is full rank:

$$\begin{bmatrix} \mathbf{A}_{\mathbf{l}_2} & \mathbf{B}_{\mathbf{l}_2} \\ \mathbf{M}^{-1}\mathbf{W}_{\boldsymbol{\tau}}\mathbf{T}_{\mathbf{l}_2}\mathbf{C}_{\mathbf{l}_2} & \mathbf{0} \\ \mathbf{N}_{\boldsymbol{\tau}}^{\mathrm{T}}\mathbf{T}_{\mathbf{l}_2}\mathbf{C}_{\mathbf{l}_2} & \mathbf{0} \end{bmatrix} = \begin{bmatrix} \mathbb{I} & \mathbf{0} & \mathbf{0} \\ \mathbf{0} & \mathbf{M}^{-1} & \mathbf{0} \\ \mathbf{0} & \mathbf{0} & \mathbb{I} \end{bmatrix} \begin{bmatrix} \mathbb{I} & \mathbf{0} \\ \mathbf{0} & \mathbf{W}_{\boldsymbol{\tau}} \\ \mathbf{0} & \mathbf{N}_{\boldsymbol{\tau}}^{\mathrm{T}} \end{bmatrix} \begin{bmatrix} \mathbf{A}_{\mathbf{l}_2} & \mathbf{B}_{\mathbf{l}_2} \\ \mathbf{T}_{\mathbf{l}_2}\mathbf{C}_{\mathbf{l}_2} & \mathbf{0} \end{bmatrix} \tag{76}$$

Since $\mathrm{Null}(\mathbf{W}_{\boldsymbol{\tau}})$ is the orthogonal complement of the column space of $\mathbf{W}_{\boldsymbol{\tau}}^{\mathrm{T}}(\boldsymbol{x})$ [41], the matrix $[\mathbf{N}_{\boldsymbol{\tau}}\ \ \mathbf{W}_{\boldsymbol{\tau}}{}^{\mathrm{T}}]$ is square and full rank for any $\boldsymbol{x} \in \mathbb{W}$. It results that the matrix in the middle of the product (76) is full rank. As the other matrices of the product are full rank, the result is full rank. Thereby, the controllability assumption holds.

3) Nominally error-free observer. Let us partition the state vector $\mathbf{x}$ into the two subsets: $\mathbf{l}_\mathbf{2}^*$ and $\mathbf{x}^- = [\dot{\boldsymbol{x}}^{\mathrm{T}}\ \boldsymbol{x}^{\mathrm{T}}\ \mathbf{x}_{\dot{\mathbf{l}}_2}{}^{\mathrm{T}}\ \mathbf{x}_{\mathbf{w_f}}{}^{\mathrm{T}}]^{\mathrm{T}}$. Consider the following form of an observer of the augmented system (47)-(49):

$$\hat{\mathbf{x}}_{k+1}^- = \boldsymbol{f}_{\mathbf{aug}}^-(\hat{\mathbf{x}}_k, \hat{\mathbf{d}}_k, \mathbf{f}_k^*) + \boldsymbol{l}_{\mathbf{x}^-}(\mathbf{y}_{\mathbf{m}k} - \boldsymbol{g}(\hat{\mathbf{x}}_k)) \tag{77}$$

$$\begin{bmatrix} \hat{\mathbf{l}}_{\mathbf{2}_{k+1}}^* \\ \hat{\mathbf{d}}_{k+1} \end{bmatrix} = \begin{bmatrix} \hat{\mathbf{l}}_{\mathbf{2}_k}^* \\ \hat{\mathbf{d}}_k \end{bmatrix} + \Delta t \begin{bmatrix} \mathbb{I} \\ \mathbf{0} \end{bmatrix} \dot{\mathbf{l}}_{\mathbf{2}_k}^* + \boldsymbol{l}_{\mathbf{dist}}(\mathbf{y}_{\mathbf{m}k} - \boldsymbol{g}(\hat{\mathbf{x}}_k)) \tag{78}$$

where $\mathbf{y_m}$ is the plant measurement vector and $\boldsymbol{f}_{\mathbf{aug}}^-$ is the vector function of output $\mathbf{x}_{k+1}^-$. The functions $\boldsymbol{l}_{\mathbf{x}^-}$ and $\boldsymbol{l}_{\mathbf{dist}}$ are the two state update functions, which have to be designed such that the observer is stable.

The observer is defined as nominally error-free at

steady state, if it satisfies [33]:

$$\forall \mathbf{e}, \quad \boldsymbol{l}_{\mathbf{dist}}(\mathbf{e}) = \mathbf{0} \quad \Longrightarrow \quad \mathbf{e} = \mathbf{0} \tag{79}$$

This assumption ensures that at steady state, the model output $\boldsymbol{g}(\hat{\mathbf{x}})$ estimated by a nominally error-free observer matches the plant measurement $\mathbf{y_m}$. The proof begins with the steady-state conditions: $\hat{\mathbf{l}}^*_{\mathbf{2}_{k+1}} = \hat{\mathbf{l}}^*_{\mathbf{2}_k}$ and $\hat{\mathbf{d}}_{k+1} = \hat{\mathbf{d}}_k$ with a velocity control $\dot{\mathbf{l}}^*_{\mathbf{2}} = 0$. Based on (78), these conditions impose $\boldsymbol{l}_{\mathbf{dist}}(\mathbf{y_{m_k}} - \boldsymbol{g}(\hat{\mathbf{x}}_k)) = \mathbf{0}$. Then, the condition (79) yields at steady state:

$$\mathbf{y_m} = \boldsymbol{g}(\hat{\mathbf{x}}) \tag{80}$$

With the EKF proposed as a state observer, the function $\boldsymbol{l}_{\mathbf{dist}}$ is replaced here by the submatrix $\mathbf{L_{dist}}$ of the Kalman filter gain. Due to the initial assumption $n_{dist} = n_y$, the matrix $\mathbf{L_{dist}}$ is square. Besides, this matrix is not singular if the filter is stable, as demonstrated in [38]. Thus the condition (79) is verified for $\mathbf{L_{dist}}$ and the EKF is a nominally error-free observer of the augmented system.

4) Nominally error-free controller. Let us define the NMPC by the function $\mathbf{c_0}$: $\mathbf{u_0}^*_k = \mathbf{c_0}(\hat{\mathbf{x}}_k, \hat{\mathbf{d}}_k, \mathbf{y_r}_k)$. The NMPC is nominally error-free at steady state, if for all admissible $\mathbf{y_r}$ and $\mathbf{d}$, yielding a feasible target $\bar{\boldsymbol{\tau}}$:

$$\mathbf{x} - \boldsymbol{f}_{\mathbf{aug}}(\mathbf{x}, \mathbf{d}, \mathbf{c_0}(\mathbf{x}, \mathbf{d}, \mathbf{y_r})) = \mathbf{0} \implies \boldsymbol{g}(\mathbf{x}) = \mathbf{y_r} \tag{81}$$

holds for all steady-state vector $\mathbf{x}$.

This assumption ensures that, when a steady state is reached, the output $\mathbf{y}$ of the nominal closed-loop system matches the reference $\mathbf{y_r}$. It is worth emphasizing that this error-free property applies only to the nominal closed loop [33], i.e. the closed loop composed of the augmented system and the NMPC using the same augmented model as its prediction model. This property alone does not result in an error-free control for the closed loop composed of the previous NMPC and the real plant (due to the mismatch between the model and the plant).

This nominal error-free assumption requires that the minimum of the cost function corresponds to a steady state with zero error with respect to the reference $\mathbf{y_r}$. Assuming closed-loop asymptotic stability of the equilibrium (81), the minimum of the positive definite cost function (50) implies [42]: $\mathbf{u_0}^* = \mathbf{0}$ and $\mathbf{y} = [\boldsymbol{x_r}^{\mathrm{T}}\, \bar{\boldsymbol{\tau}}^{\mathrm{T}}]^{\mathrm{T}} = \mathbf{y_r}$ at steady state, where $\bar{\boldsymbol{\tau}}(\boldsymbol{x_r}, \mathbf{d})$ is a solution of the CDPR kineto-static equation (56).

Finally, let us consider the closed loop composed of the real plant, the previous NMPC and previous EKF observer. It is assumed (Assumption 1 in [33]) that, for an asymptotically constant reference ($\mathbf{y_r}_k \to \mathbf{y_r}_\infty$ when $k \to \infty$) and constant external disturbance, all the states of this closed loop converge to steady values with $\mathbf{y_m}_k \to \mathbf{y_m}_\infty$ and $\mathbf{u}_k \to \mathbf{u}_\infty$.

The offset-free property of the controller can be proved with Theorem 4 in [33], which is restated as:

a) the observability assumption holds with $n_{dist} = n_y$. It is tested locally for the cable-thruster actuated CDPR with Theorem 2 from [33].
b) the controllability assumption holds for the cable actuation with $n_{y_c} = n_\tau$, as tested locally via the Theorem 3 from [33].
c) the error-free observer assumption holds for the proposed EKF filter. (Because of a), it is possible to design such an observer.)
d) the assumption of a nominally error-free NMPC holds. (Because of b), it is possible to design such a controller).

therefore $\mathbf{y_m}_k \to \mathbf{y_r}_k$ when $k \to \infty$, i.e. the control is offset-free.

Let us summarize the outline of the theorem proof: with the closed-loop convergence to a steady state assumption, it is sufficient to prove that $\mathbf{y_m}_\infty = \mathbf{y_r}_\infty$ [33]. First, from the output $\mathbf{u_0}^*_\infty = \mathbf{c_0}(\hat{\mathbf{x}}_\infty, \hat{\mathbf{d}}_\infty, \mathbf{y_r}_\infty)$ of the NMPC at steady state and from d), it comes $\boldsymbol{g}(\hat{\mathbf{x}}_\infty) = \mathbf{y_r}_\infty$ (81). Then, from c) comes $\mathbf{y_m}_\infty = \boldsymbol{g}(\hat{\mathbf{x}}_\infty)$ (80). These last two equalities result in $\mathbf{y_m}_\infty = \mathbf{y_r}_\infty$.

The offset-free control and control allocation are validated in the next section through simulations and experiments on a planar cable-thruster actuated CDPR.

4. Experimental Validation

4.1. Experimental Setup

4.1.1. PiSaRo4 Robot

A planar suspended CDPR robot with 3 cables and 4 onboard propeller-based thrusters (Fig. 5) is considered to validate the proposed control. The platform of this robot, called PiSaRo4, is composed of a square aluminum frame on which all the actuators, electronics and power sources are embedded.

This robot is designed to perform tasks on vertical surfaces like maintenance and painting on the exterior walls of buildings. The winches and actuators are embedded on the platform similarly to CDPRs used for solar panel [43] or facade cleaning [44], [8]. This design simplifies the installation and disassembly of the system: it avoids having to attach and to power winches that are scattered on the edges of the workspace. The

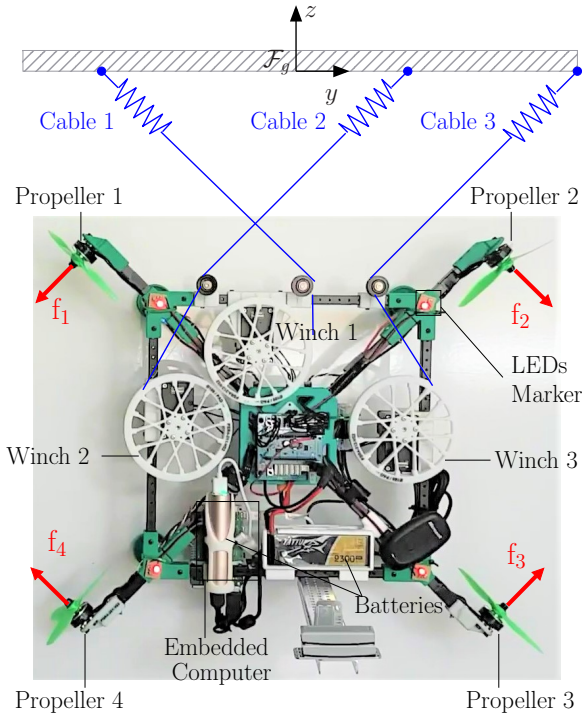

Fig. 5: PiSaRo4 CDPR with onboard propeller-based thrusters.

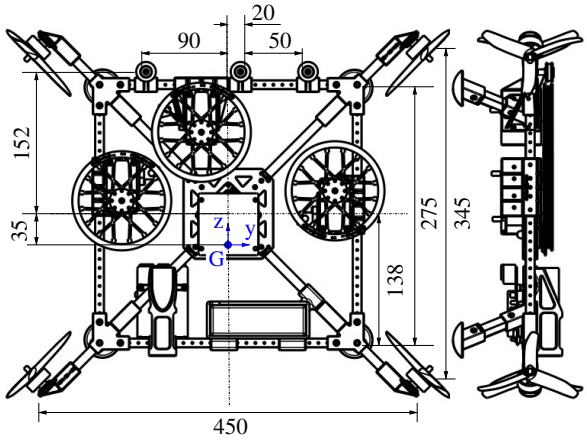

Fig. 6: Font and side CAD views of the PiSaRo4. The dimensions with respect to the centre of gravity G specify the positions of the thrusters and the cable outputs on the idler pulleys. All dimensions are given in mm.

drawback of this design is an additional weight on the moving platform. The actuators and the cable stored in the winches are the main sources of the weight increase, especially if the cable is made of steel [44]. To reduce this weight, lightweight but elastic cables made of polyamide are considered in [44] as well as here for the PiSaRo4.

With a suspended configuration, only three cables are required to control the 3 DoFs of this planar robot (the gravity acts as a fourth cable). The out-of-plane motion of the platform is constrained by the contacts between the wall and the four legs on the back of the PiSaRo4 robot (see the CAD side view in Fig. 6). The arrangement of the three cables on the PiSaRo4 is based on the 3-DoF planar kinematics proposed in [45]. Regarding the onboard thrusters, their initial purpose was to efficiently damp the vibration of the platform along all the DoFs. To generate a wrench along $n = 3$ DoFs, at least $n + 1 = 4$ unidirectional thrusters are necessary. This condition is identical to the condition on the number of cables for a fully-constrained CDPR [5]. The symmetric configuration of the four thrusters and their position on each corner of the platform are shown in Fig. 6. This configuration maximizes the thruster-feasible wrench in all the directions. It is directly inspired from the configuration commonly used to control the motion of unmanned underwater vehicles in the horizontal plane [46].

To drive the three winches of radius 51 mm, three DYNAMIXEL XM540-W150 servomotors are attached to the platform frame. Inside the DYNAMIXEL, a digital velocity control loop regulates the winding speed of the cable. The maximum winding speed is $\dot{l}_{2\,\max} = 0.26\,\mathrm{m.s^{-1}}$ based on the winch radius and servomotor speed limit. A settling time of 100 ms has been measured for this velocity loop. A second-order transfer function $G_{\dot{l}_2}(s)$ is identified as the winch velocity dynamics. Its damping ξ and natural pulsation ω_n are given in Table 1 with the other parameters of the model.

Three polymer cables (Reactive Tackle Hi Vis Yellow 300LB) run from their winding winch to a pulley on top of the platform, such that the exit point of each cable stays constant with respect to the platform frame. From these pulleys, the cables run to their anchoring points on the supporting structure (Fig. 5). The PiSaRo4 kinematics is defined by its anchoring point coordinates ${}^g\mathbf{a}_{\tau_1} = [-1.55\ 0]^{\mathrm{T}}$, ${}^g\mathbf{a}_{\tau_2} = [1.55\ 0]^{\mathrm{T}}$, ${}^g\mathbf{a}_{\tau_3} = [1.77\ 0]^{\mathrm{T}}$ and pulley outputs ${}^b\mathbf{b}_{\tau_1} = [0.02\ \ 0.187]^{\mathrm{T}}$, ${}^b\mathbf{b}_{\tau_2} = [-0.09\ 0.187]^{\mathrm{T}}$, ${}^b\mathbf{b}_{\tau_3} = [0.07\ 0.187]^{\mathrm{T}}$m.

To emulate the low stiffness of long cables in the restricted space of a laboratory room, a spring is inserted

Parameter	Description	Value	Unit
m_b	Robot mass	2.58	kg
I_b	Robot inertia along x	0.058	kg.m^2
k_{a1}	Spring stiffness	27	N.m^{-1}
k_{a2}	Spring stiffness	13.5	N.m^{-1}
k_{a3}	Spring stiffness	13.5	N.m^{-1}
ξ	Winch damping coefficient	0.78	-
ω_n	Winch natural pulsation	32.4	rad.s^{-1}
T_f	Thruster time constant	0.035	s

Table 1: PiSaRo4 parameters.

between the anchoring points and the cable ends. The stiffness of the cable+spring assembly is approximated by the stiffness of the spring alone. Indeed, the stiffness of springs in series, where one spring has a significant lower stiffness than all other springs, is approximately equal to this lowest stiffness. By solving the PiSaRo4 kineto-static problem (57) at the nominal pose of the platform $\bar{\boldsymbol{x}} = [y\ z\ \theta]^\mathrm{T} = [0\ -1.7\ \ 0]^\mathrm{T}$, it appears that the tension of the cable 1 (18.8 N) is twice the tension of the other cables (10.3 N and 7.9 N). To avoid exceeding its elastic range, the stiffness k_{a_1} of the spring 1 is doubled (by an assembly of two springs in parallel).

The four embedded thrusters generate unidirectional thrusts and are driven by electronic speed controllers (ESC). Since a standard ESC does not accurately regulate the rotational velocity of the propeller and since the propeller thrust is proportional to the square of this velocity, a fast speed regulation is implemented: a digital PID regulation of the propeller speed using the ESC real-time telemetry data is implemented on a Teensy3.5 microcontroller (source code available at `https://github.com/jacqu/teensyshot`). The PID parameters are tuned to achieve a step response to a thrust reference as close as possible to a first order response of time constant $T_\mathrm{f} = 0.035$ s. The maximum thrust of one propeller is 6.7 N at full speed, limited to $\mathrm{f}_{\max} = 3.8$ N for the experiments due to safety concerns. Based on the time constant, the force bandwidth of the thruster is 4.5 Hz. By comparison, the bandwidth of the cable actuation for a nominal 3 N tension is 0.33 Hz considering the stiffness k_{a2}, the winch dynamics and its velocity saturation. Note that the bandwidth of cable actuation depends on the desired force amplitude due to the nonlinear effect of the saturation.

The pose $\boldsymbol{x} = [y, z, \theta]^\mathrm{T}$ of the CDPR is measured by an exteroceptive sensor: a distant Ximea xiQ USB camera running at 500 Hz and subsampled to 100 Hz by the controller. By detecting the 4 red LEDs (Fig. 5) mounted on the CDPR platform, the pose is extracted from the camera image. A remote computer handles the image processing as well as the NMPC computation.

The onboard Raspberry Pi 4 computer acts mainly as a communication hub. It manages data exchange between the remote computer connected over WiFi and the actuators (winches and thrusters) connected to the Raspberry Pi through USB. Finally, a 3S Lipo battery (11,1V) provides power to the winch servomotors and thrusters. The Raspberry Pi board is powered by a 5V power bank battery. The total mass of the PiSaRo4 robot is 2.58 kg.

4.1.2. Controller Implementation

To evaluate the benefit of a hybrid actuation, two NMPC are designed for the PiSaRo4: one NMPC with cable actuation only and a second NMPC with hybrid cable-thruster actuation. The prediction model is derived from continuous-time dynamic model (37) considering a 3-DoF CDPR with 3 cables for the first NMPC and 3 cables with 4 additional thrusters for the second. The actuator models are the second-order model for the winch actuators and the first-order model for the thrusters described in the previous subsection 4.1.1. The dynamic model with the cable-only actuation has 15 states, while the model with the additional thrusters has 19 states.

The PiSaRo4 CDPR has no redundant cable ($n = n_\tau = 3$). Thereby, according to Section 3.3, the cable tension can be removed from the OCP cost function (50) and the measurement vector $\mathbf{y}$ is only composed of the pose $\boldsymbol{x}$. Furthermore, augmenting the model of the PiSaRo4 with a constant disturbance $\mathbf{d}$ is not required to satisfy the offset-free initial assumption: $n_{dist} = n_y$. Indeed, the estimate $\hat{\mathbf{l}}_\mathbf{2}^*$ of the n_τ cable free lengths is sufficient to gather any model uncertainties or unmodeled disturbances, as detailed in the beginning of section 3.4. The rank conditions for the offset-free observability (61) and controllability (72) assumptions are readily adapted and verified for the non-redundant case: the tension ($\mathbf{T_x}$ and $\mathbf{T_{l_2}}$) and disturbance ($\mathbf{F_d}$) Jacobians are removed from the matrices while the matrix $\mathbf{W_\tau}$ becomes square and full rank.

An EKF provides the full state estimate $\mathbf{x_0} = \hat{\mathbf{x}}_k$, which includes the estimate $\hat{\mathbf{l}}_\mathbf{2}^*$. The block diagram of the corresponding NMPC closed loop is depicted in Fig. 7.

The NMPC is implemented using the open-source toolkit `acados` [40]. This software allows for a high-level description of an OCP and generation of self-contained C code to solve the problem efficiently. With

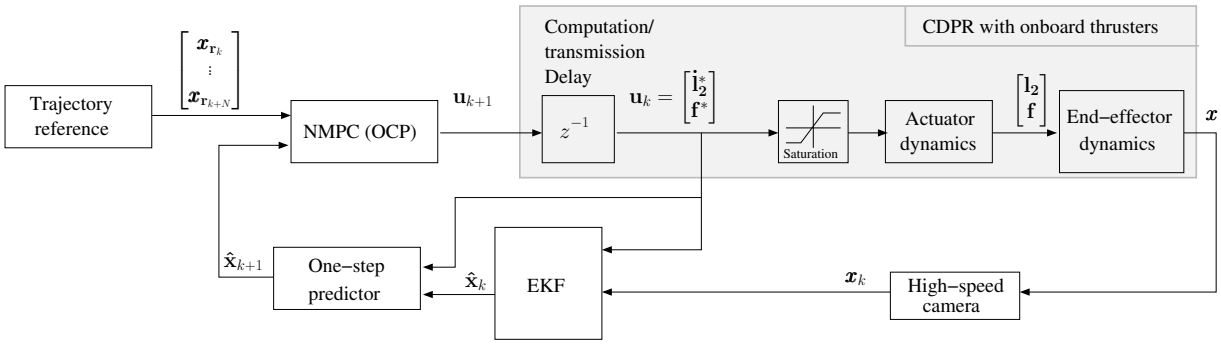

Fig. 7: NMPC control of the PiSaRo4 CDPRs with on-board thrusters, and with compensation of the computational and transmission delay of the control signal.

Parameter	Value	Unit
T, Horizon time length	1	s
N, Horizon steps	50	-
$\mathbf{Q_y}$, Pose error penalty	diag([1, 1, 0.3])	-
$\mathbf{Q_{\dot{l}_2}}$, Winch velocity penalty	$2.10^{-4}\,\mathbb{I}_3$	-
$\mathbf{Q_f}$, Thrust penalty	$2.10^{-5}\,\mathbb{I}_4$	-
$\dot{l}_{2\,\max}$, max. winding speed	0.26	$\mathrm{m.s^{-1}}$
$\tau_{\max}$, max. cable tension	202	N
$\mathrm{f_{min}}$, minimum thrust	0.0	N
$\mathrm{f_{max}}$, maximum thrust	3.8	N

Table 2: NMPC parameters.

a warm startup scheme and a state-of-the-art quadratic programming solver (HPIPM [40]) embedded in the generated C-code, computation of the NMPC solution can be achieved in real time.

Within `acados`, the continuous-time plant model (37) is discretized using a multiple shooting method and a Runge-Kutta integration [40] to solve the nonlinear differential equations of the PiSaRo4 dynamics. For a deterministic runtime, fixed order and step Runge-Kutta methods are preferred in `acados` and are currently the only ones available. The tuning parameters of the NMPC are summarized in Table 2.

The penalty weights $\mathbf{Q_y}$ and $\mathbf{Q_u} = \mathrm{blkdiag}(\mathbf{Q_{\dot{l}_2}}, \mathbf{Q_f})$ of the OCP cost function (50) are initially tuned in simulations. The tuning starts with the cable-only NMPC. The tuning criterion is the minimization of the 5% settling times, when tracking the reference steps in Fig. 9. The weight on each DoF position is first normalized to 1, such that $\mathbf{Q_y} = \mathbb{I}_3$. Next, a weight $\mathbf{Q_{\dot{l}_2}}$ on the winch control signals of the form $\mathbf{Q_{\dot{l}_2}} = q_{\dot{l}_2}\,\mathbb{I}_3$ that minimizes the sum of the settling times is searched. Using an interval halving (bisection) method, a shared weight $q_{\dot{l}_2} = 4.10^{-4}$ is found that does not favor a winch over another. Freezing the previous weights, a weight $\mathbf{Q_f} = 7.10^{-5}\,\mathbb{I}_3$ on the thruster control signals is found for the NMPC with hybrid actuation by considering the same criterion. Finally, using these weights as an initial guess, they are finely tuned on the experimental robot (see Table 2) with an interval halving method requiring several trials.

The length of the prediction horizon is $T = 1$s, long enough to span the closed-loop response observed during the experiments. To reduce the size and computation time of the optimization problem, the sampling time on the prediction horizon is set to 20 ms resulting in $N = 50$ horizon steps. However, the OCP is solved at the closed-loop sampling period of T_s =10 ms, such that $\mathbf{x_0}$, the initial state of the OCP, is updated with the latest pose measurement feedback from the camera.

The NMPC generated C-code runs on a remote PC with an i5-9500 processor. At each period T_s, the OCP solution $\mathbf{u_0^*} = [\mathbf{\dot{l}_2^{*T}}, \mathbf{f^{*T}}]^{\mathrm{T}}$ is sent over WiFi (5 GHz channel to minimize the delays) to the winch servomotors and propeller ESCs as the reference of their inner velocity loops. The computation time to solve the OCP for the model with hybrid cable-thruster actuation is measured during the experiments. Its mean value is 2.35 ms with a peak at 5.4 ms.

A one-period delay is introduced in the control loop by the computation time and the latency of the wireless transfer of the optimal control solution between the remote PC and the CDPR. As a consequence, the control signal sample is applied on the system at the beginning of the next time step.

If this delay is not taken into account, the robustness of the control might decrease as noticed during simulations and the experiments (see section 4.3.1). A common approach to compensate for this delay is to use a one-step predictor in the control loop [47]. As

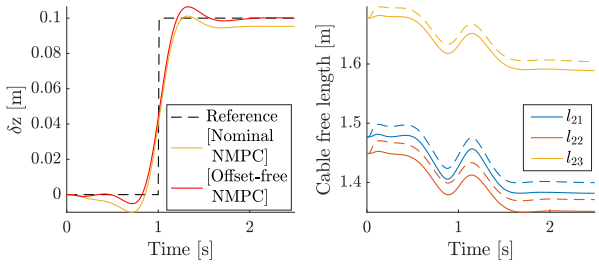

Fig. 8: On the left, step responses of the nominal NMPC and offset-free NMPC for an inaccurate value of the CDPR mass. On the right, corresponding cable free lengths $\mathbf{l_2}$ (solid lines) versus the estimated lengths $\hat{\mathbf{l}}_2^*$ (dashed lines).

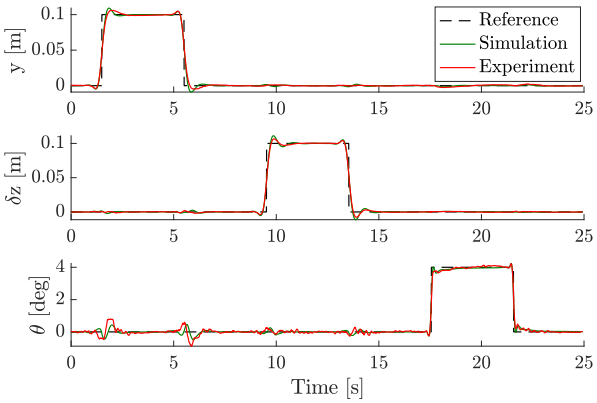

Fig. 9: Simulated and experimental step responses on each DoF.

illustrated in the diagram of Fig. 7, using a predictor (forward RK4 integration), the state estimate $\hat{\mathbf{x}}_{k+1}$ can be used as the initial state for the OCP problem. The output of the NMPC is thus the control signal $\mathbf{u}_{k+1}$, one step ahead of the current sample time. By predicting the state $\hat{\mathbf{x}}_{k+1}$ outside of the NMPC, the OCP formulation does not change between the delayed and undelayed cases [47] and a delay-free model can still be used.

4.2. *Offset-free Steady State and Model Validation*

To validate the offset-free control, a simulation is carried out introducing a 2.5 % error (64.5 g) on the platform mass in the PiSaRo4 dynamic model.

The proposed offset-free NMPC is compared to a nominal NMPC. The nominal NMPC uses the measurement of the cable free lengths $\mathbf{l_2}$ from the plant to initialize the OCP. However, the offset-free NMPC uses the estimate $\hat{\mathbf{l}}_2^*$ from the EKF observer.

The results of step response simulations along the z axis are given in Fig. 8, where δz represents the robot displacement relative to the equilibrium pose $\bar{\boldsymbol{x}} = [0 \quad -1.7 \quad 0]^{\mathrm{T}}$. It confirms that the offset-free NMPC achieves a zero steady-state error, while the nominal NMPC does not. The constant disturbance due to the mass error is identified and included in the estimate $\hat{\mathbf{l}}_2^*$ by the EKF. It is visible in the difference between the cable free lengths $\mathbf{l_2}$ (solid lines) and its estimates $\hat{\mathbf{l}}_2^*$ (dashed lines in the right plot of Fig. 8).

The cable length difference is $\hat{\mathbf{l}}_2^* - \mathbf{l_2} = [0.018 \quad 0.02 \quad 0.015]^{\mathrm{T}}$m at the final steady state. Considering the cable directions at the steady-state pose $\boldsymbol{x} = [0 \quad -1.6 \quad 0]^{\mathrm{T}}$ and the cable stiffnesses from Table 1, the disturbance force is 0.633 N, corresponding to 64.5 g, matching the error on the platform mass.

To validate the PiSaRo4 model accuracy, simulation and experimental step responses are compared for each DoF of the robot. The comparison can be seen in Fig. 9 where both experimental and simulation plots fit well, thus validating the dynamic model. However, the simulation exhibits greater overshoots than the experiments. This slight discrepancy is likely due to frictions neglected in the model and an inaccurately identified cable stiffness. The cable stiffness is a sensitive parameter: its value directly impacts the magnitude of the tensile force exerted on the platform.

4.3. *Experimental Results*

Several experiments were conducted using the PiSaRo4 robot without (denoted as '*cable only*' hereafter) and with the thruster actuation ('*cable + thruster*') to assess the impact of thrusters on the robot performance. All the experiments use a preview of the CDPR pose reference signal on the prediction horizon. The preview improves the tracking with NMPC control signals anticipating the change of reference.

4.3.1. *Step Responses*

The performance of hybrid cable-thruster actuation is first assessed with step responses on each DoF.

As shown in Fig. 10, the robot dynamics are improved by the use of thrusters. Thanks to their additional wrench and the higher bandwidth, the rise and settling times are improved with thrusters (Table 3). The 5% settling time is improved in a range going from 7% for the orientation θ to 29% for the horizontal translation y. The rise time, defined by the time from 10% to 90% of the final value, is also improved from 28% for the vertical translation z to 68% for the orientation θ.

The rise-time discrepancy between the DoFs is due to the speed saturation of the winch actuators. When the length of cables to be wound is significant, the winch

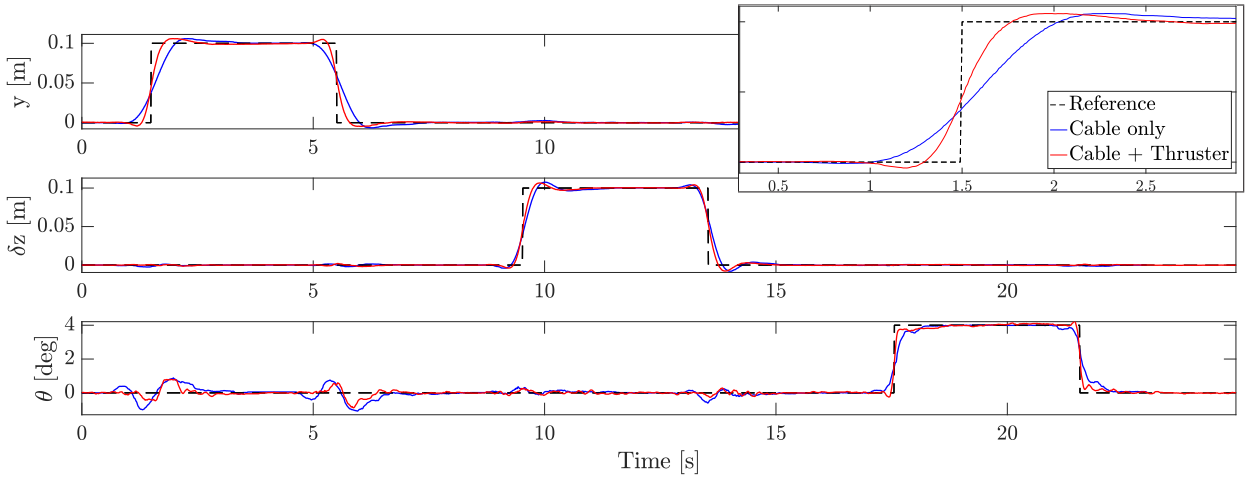

Fig. 10: Step responses on each DoF with and without thrusters. On top right, zoom on the step response along y axis.

	Cable only			Cable + Thruster		
	y	z	θ	y	z	θ
Overshoot [%]	5 .9	7.6	-	5.9	6.5	-
Settling Time [s]	0.92	0.61	0.55	0.65	0.45	0.51
Rise Time [s]	0.65	0.40	0.37	0.31	0.29	0.12

Table 3: Step responses characteristics on each DoF: cable only versus cable-thruster actuation.

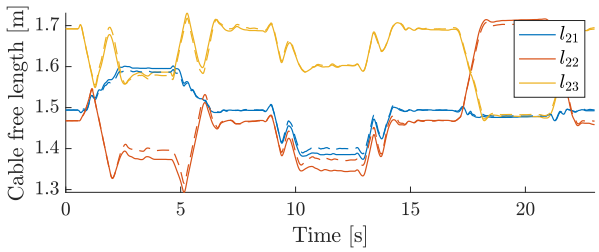

Fig. 11: Cable free lengths for the step trajectory with cable-only actuation: cable lengths $\mathbf{l_2}$ from winch encoders (solid lines) versus estimated lengths $\hat{\mathbf{l}}_2^*$ from the EKF observer (dashed lines).

control signal is clipped yielding a significant lower response time without the additional thrust of the propellers. As visible in Fig. 11, the longest cable length to wind is for the rotation. Thus, orientation control is significantly improved with thrusters, where the rise time is 3 times shorter than without thrusters.

The clipped portion of the winch velocity due to saturation is reduced with hybrid cable-thruster actuation compared to the cable only case (see Fig. 12). The control signals for the orientation step at $t = 17.5\,\text{s}$ has a noticeable slope: the NMPC promotes thrusters instead of winches to achieve a quick transient and maintain the new orientation (see Fig. 12b). However, the thruster control signal decreases linearly over time, indicating that the controller is progressively shifting from thrusters to winches in order to maintain a steady state, thus saving energy. This behavior is confirmed by the cable tensions, proportional to the cable elongations, in Fig. 13. With thrusters, the cable tensions for the orientation step at $t = 17.5\,\text{s}$ converge slowly to their final value compared to the cable only case. Thanks to a preview of the reference in the optimization horizon, the reference is anticipated reducing the tracking error: at the step time, half of the step amplitude has already been traveled by the system.

These first results confirm the NMPC ability to efficiently handle the allocation problem. The NMPC achieved optimal tracking performance while distributing the wrench between winches and thrusters. The full velocity of the winches is used both with and without the thruster actuation. As expected, the penalty on the thrust control in the cost function yields a thrust tending towards zero at steady state. Moreover, the tracking is achieved while enforcing – the saturation constraint on the actuator control signals (Fig. 12) and – the positivity constraint on the cable tensions (Fig. 13). The mean and maximal cable tensions are similar with and without the thruster actuation, as visible in Fig. 13.

With and without the thruster actuation, the step responses reach an offset-free steady state. To achieve this offset free tracking, constant disturbances in the model are estimated online to capture the mismatch (on the cable stiffness, on the kinematic parameters,...) between the PiSaRo4 system and the model at steady state. Here, the constant disturbances are lumped into the cable length $\hat{\mathbf{l}}_2^*$ estimated by an EKF. In Fig. 11, these constant disturbances are visible in the difference between $\mathbf{l_2}$ and its estimate $\hat{\mathbf{l}}_2^*$ from the EKF at steady

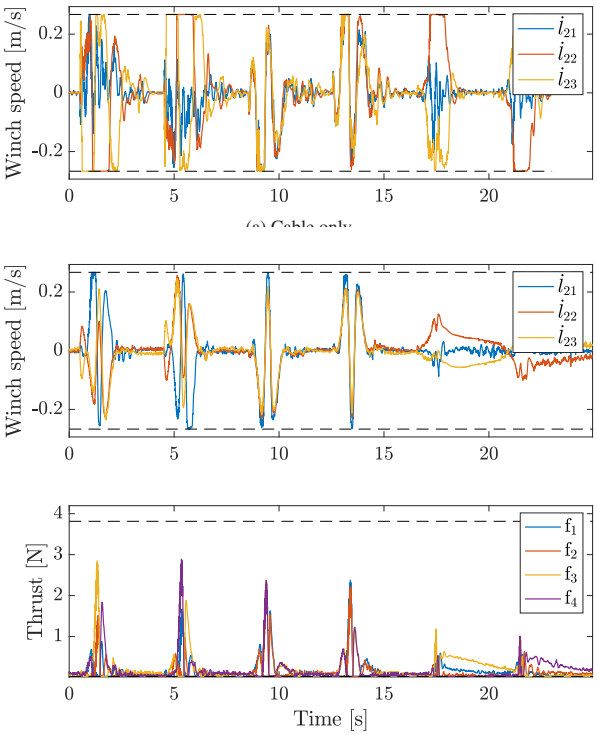

(b) Cable + Thruster

Fig. 12: Actuator control inputs for the step trajectory: cable only a) versus cable-thruster b) actuation. The dashed black lines show the actuator saturation limits.

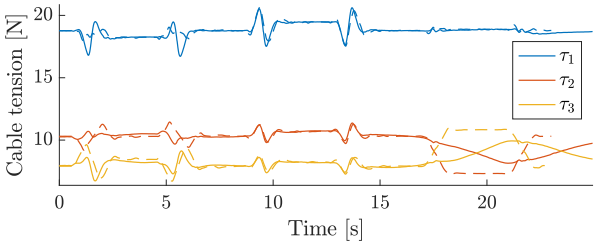

Fig. 13: Cable tension for the step trajectory: cable only (dashed lines) versus cable-thruster (solid lines) actuation.

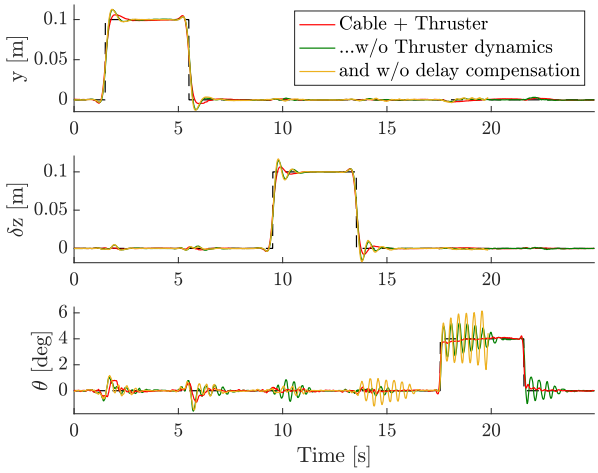

Fig. 14: Step responses -with thruster dynamic model, -without thruster dynamic model and -without thruster dynamics model and delay compensation.

state.

Lastly, experiments were carried out to assess the relevance of modeling the fast dynamics of the thrusters by removing these dynamics from the plant model. Therefore, the effective thrust is assumed to be instantaneously equal to its control reference signal. Step responses in Fig. 14 show that the performance deteriorates if the first-order dynamics of the thruster is omitted in the prediction model: the overshoot doubles on the translations while the damping of the orientation response decreases. However, the mean computation time of the OCP solution is reduced from 2.16 ms for the full model to 1.93 ms (-11%) for the model without the thruster first-order dynamics. If both the thrust dynamics and the delay compensation of the control computation time are omitted (removing the one-step prediction block in Fig. 7), the orientation control becomes unstable and the experiment has to be stopped at t=20 s (Fig. 14). In conclusion, the thruster dynamics have to be taken into account in the controller to achieve the best performance.

4.3.2. Trajectory Tracking

A trajectory composed of – a six-sided polygon for the position and – a constant null angle for the orientation is considered. The slow and the fast version of the trajectory passing through 6 waypoints are characterized by a mean velocity of 0.05 $m.s^{-1}$ and 0.15 $m.s^{-1}$ respectively. The corresponding pose of the PiSaRo4 as a function of time is computed offline using a fifth-order polynomial trajectory generator.

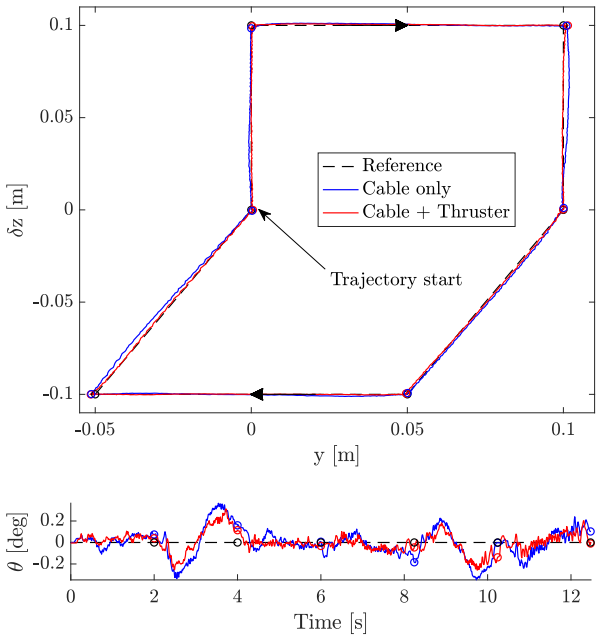

Fig. 15: Trajectory tracking at 0.05 m.s^{-1}: cable only versus cable-thruster actuation. Position trajectory at the top and constant orientation trajectory at the bottom.

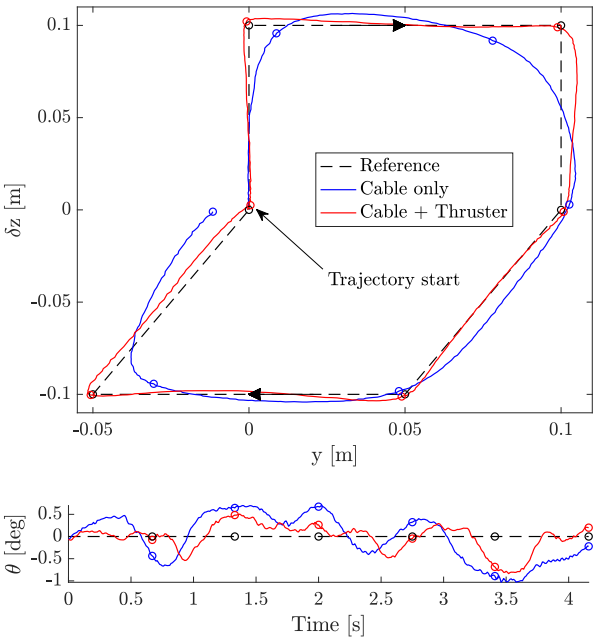

Fig. 16: Trajectory tracking at 0.15 m.s^{-1}: cable only versus cable-thruster actuation. The circles on the trajectories indicate poses reached at the same time instant, as visible in the orientation plot.

	RMS error		Max error	
	d	θ	d	θ
Cable only	2.3 mm	0.13 °	5.9 mm	0.37 °
Cable + Thruster	1.2 mm	0.09 °	3.4 mm	0.31 °
Improvement	47%	31%	42%	15%

Table 4: Position d and orientation θ trajectory tracking error at 0.05 m.s^{-1}: cable only versus cable-thruster actuation.

	RMS error		Max error	
	d	θ	d	θ
Cable only	15.3 mm	0.51 °	32.0 mm	1.03 °
Cable + Thruster	5.4 mm	0.30 °	9.3 mm	0.84 °
Improvement	65%	41%	71%	19%

Table 5: Trajectory tracking error in position d and orientation θ trajectory tracking error at 0.15 m.s^{-1}: cable only versus cable-thruster actuation.

For the low-speed trajectory, the hybrid cable-thruster actuated CDPR exhibits better tracking performance than the cable only actuated CDPR, as shown in Fig. 15. The tracking error at each change of direction decreases notably when using the thrusters. While the actuator saturations are never reached for this slow trajectory (control signals are displayed later for the fast trajectory), the higher bandwidth of the thrusters contributes to an improvement in the tracking accuracy. This accuracy is improved up to 31% for the orientation and 47% for the position when considering the RMS error along the trajectory (see Table 4). The position error is defined by the distance d between the CDPR and the reference position at time t. The maximum of this error along the whole trajectory is also reduced from 5.9 mm to 3.4 mm when adding the thrusters.

Nevertheless, the improvement of the performance is more significant as the trajectory speeds up and the actuator saturations are reached. Without thrusters, the CDPR position lags behind the reference (Fig. 16). The CDPR position is unable to keep up with the trajectory despite the anticipation feature of the NMPC. On the other hand, the system with hybrid cable-thruster actuation can keep up with the trajectory (Fig. 16). The total duration of the winch saturation phases is divided by more than two with the thrusters (Fig. 17b) while the RMS position error along the trajectory is reduced by 65% and by 41% for the orientation with the contribution of the thrusters (Table 5). The maximum position error is also reduced by a similar ratio from 32 mm to 9.3 mm.

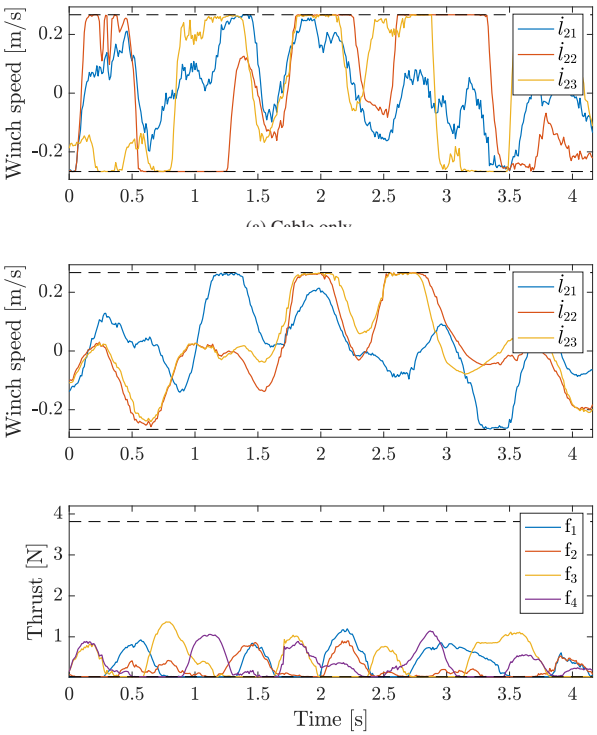

(b) Cable + Thruster

Fig. 17: Actuator control inputs for the $0.15\,\mathrm{m.s^{-1}}$ trajectory: cable only a) versus cable-thruster b) actuation. The dashed black lines show the actuator saturation limits.

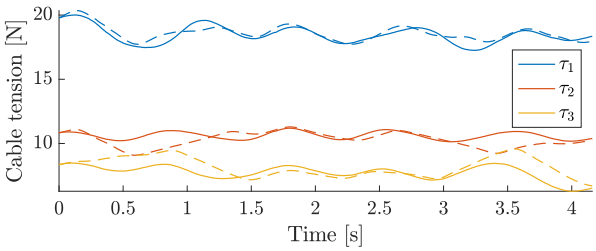

Fig. 18: Cable tension for the $0.15\,\mathrm{m.s^{-1}}$ trajectory: cable only (dashed lines) versus cable-thruster (solid lines) actuation.

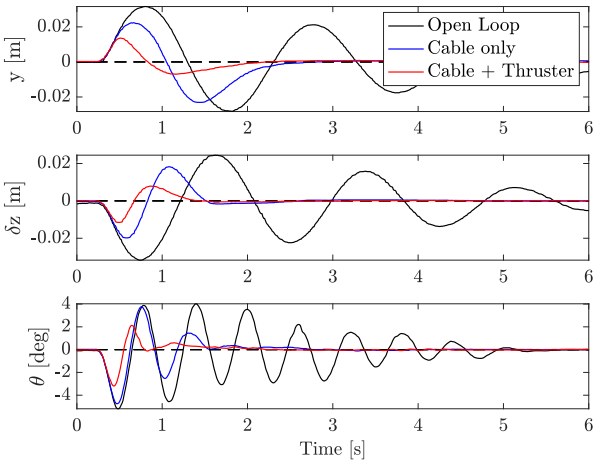

Fig. 19: Disturbance rejection comparison in open loop, with cable only and with cable-thruster actuation for an impulsive disturbance on each DoF.

Taking into account in a predictive way the saturation of the cable-thruster actuators, the NMPC achieves an effective control allocation and tracking of demanding trajectories. Even with a fast trajectory and lasting saturation of the winch actuators, the positivity constraint on the cable tensions is always satisfied (Fig. 18).

4.3.3. Disturbance Rejection

Disturbance rejection performance is tested with and without thruster actuation and compared to the open-loop response in Fig. 19. A short thrust pulse is used to generate a transient and repeatable disturbance on the resting CDPR along each DoF direction. The duration of the pulse is 200 ms and the amplitudes of the disturbances are 2 N and 0.4 N.m along the translation and rotation DoF, respectively.

The use of thrusters increases significantly the disturbance rejection capabilities of the robot as shown in Fig. 19 and Table 6 for each DoF separately. Thrusters allow for a 36 %, 40 % and 33 % decrease of the amplitude of the peak error along y, z, and θ respectively compared to the robot with cable-only actuation; and for a 56 %, 63 % and 38 % decrease when compared to the open-loop response.

	Peak Time [s]			Peak Value [mm,°]		
	y	z	θ	y	z	θ
Open Loop	0.81	0.73	0.48	31.6	31.7	5.2
Cable Only	0.66	0.57	0.47	22.4	19.8	4.8
Cable+Thruster	0.51	0.50	0.43	13.6	11.5	3.2

Table 6: Disturbance rejection assessment per axis in open loop, with cable only and with cable-thruster actuation.

A supplementary video of all the previous experiments with the PiSaRo4 CDPR and its hybrid cable-thruster actuation is available.

5. Conclusion

In this article, thrusters embedded on the platform of CDPRs are considered to improve the system dynamics. An offset-free NMPC is introduced to control the pose

and resolve the actuation redundancy of CDRP with a hybrid actuation: cable winches and onboard thrusters. NMPC is a relevant choice to control such CDPR since it solves in one optimal problem (OCP) the control allocation of the actuators and it takes into account their different dynamics, their saturation and the positivity constraints of the cable tension.

To achieve better pose tracking performance, the actuator dynamics (including the thruster fast dynamics) need to be included in the system model for the OCP. An augmented model involving constant disturbances and an alternative model of the thruster actuation are proposed. After verifying some conditions, this model achieves a zero pose tracking error at steady state while minimizing the number of states of the model. Experiments confirm that a hybrid actuation with NMPC allocation improves the tracking of pose trajectories and the damping of CDPR platform vibration. With their short response time, the thrusters can compensate for the reduced bandwidth of the winches when the cable stiffness or the limit on the winding velocity is low.

This work and its experiments have focused on hybrid-actuated CDPR with a number of cables greater than or equal to the desired number of DoFs ($n_\tau \geq n$), such that the thrusters stay inactive at steady state. However, by defining appropriate thrust and cable tension targets for the steady state, the proposed control can be extended to new robot designs: – CDPR where several cables are replaced by propellers to reduce cable self-collisions and collisions with the environment [31], or – suspended aerial manipulators where all the cables are replaced by thrusters except cables that compensate for the gravity [21] [24].

Appendix A. Alternative Model of the Thruster Actuation

Let us consider initially that G_f is a first order transfer function with one pole $\lambda_1 = -\frac{1}{T_\mathrm{f}}$. Thereby, using (13)-(14) yields the following state-space model of the actuation system with n_f identical thrusters:

$$\dot{\mathbf{x}}_\mathbf{f} = -\frac{1}{T_\mathrm{f}}\mathbb{I}_{n_\mathrm{f}}\,\mathbf{x}_\mathbf{f} + \mathbb{I}_{n_\mathrm{f}}\mathbf{f}^* \tag{A.1}$$

$$\mathbf{w}_\mathbf{f} = \mathbf{W}_\mathbf{f}(\boldsymbol{\theta})\,\frac{1}{T_\mathrm{f}}\mathbb{I}_{n_\mathrm{f}}\,\mathbf{x}_\mathbf{f} \tag{A.2}$$

For the derivation of the alternative model, consider the change of state variables $\mathbf{x}_{\mathbf{w_f}} = \mathbf{W}_\mathbf{f}(\boldsymbol{\theta})\,\mathbf{x}_\mathbf{f}$. From the definition of $\mathbf{W_f}$ (7) and the rotation matrix derivative $\dot{\mathbf{R}}_{gb}(\boldsymbol{\theta}) = [{}^g\boldsymbol{\omega}]_\times \mathbf{R}_{gb}(\boldsymbol{\theta})$ [34], it yields:

$$\dot{\mathbf{x}}_{\mathbf{w_f}} = \mathbf{W_f}\,\dot{\mathbf{x}}_\mathbf{f} + \dot{\mathbf{W}}_\mathbf{f}\,\mathbf{x}_\mathbf{f} \tag{A.3}$$

$$= \mathbf{W_f}\,\dot{\mathbf{x}}_\mathbf{f} + \left[\begin{bmatrix}[{}^g\boldsymbol{\omega}]_\times & \mathbf{0}\\ 0 & [{}^g\boldsymbol{\omega}]_\times\end{bmatrix}\mathbf{W_f}\right]\,\mathbf{x}_\mathbf{f} \tag{A.4}$$

$$= \mathbf{W_f}\,\dot{\mathbf{x}}_\mathbf{f} + \begin{bmatrix}[{}^g\boldsymbol{\omega}]_\times & \mathbf{0}\\ 0 & [{}^g\boldsymbol{\omega}]_\times\end{bmatrix}\mathbf{x}_{\mathbf{w_f}} \tag{A.5}$$

with $[{}^g\boldsymbol{\omega}]_\times$, a skew-symmetric matrix whose entries are the coordinates of ${}^g\boldsymbol{\omega}$ as defined in [34].

By left-multiplying (A.1) by $\mathbf{W_f} \in \mathbb{R}^{n\times n_\mathrm{f}}$, and substituting the new state variables and expression (A.5) in the equation, the following model is obtained:

$$\dot{\mathbf{x}}_{\mathbf{w_f}} = \left[-\frac{1}{T_\mathrm{f}}\mathbb{I}_n + \begin{bmatrix}[{}^g\boldsymbol{\omega}]_\times & \mathbf{0}\\ 0 & [{}^g\boldsymbol{\omega}]_\times\end{bmatrix}\right]\mathbf{x}_{\mathbf{w_f}} + \mathbb{I}_n\,\mathbf{W_f}(\boldsymbol{\theta})\,\mathbf{f}^* \tag{A.6}$$

$$\mathbf{w_f} = \frac{1}{T_\mathrm{f}}\mathbb{I}_n\,\mathbf{x}_{\mathbf{w_f}} \tag{A.7}$$

If $\boldsymbol{\omega} = 0$ or $\|\boldsymbol{\omega}\|_2 \ll \|\frac{1}{T_\mathrm{f}}\|_2$, the term $[\boldsymbol{\omega}]_\times$ in (A.6) vanishes or can be neglected leading to the alternative model (20)-(21).

To generalize the model derivation for a transfer function G_f of order m_f, let us consider a diagonal form of the state-space representation (13)-(14):

$$\dot{\mathbf{x}}_\mathbf{f} = \mathbf{J_f}\,\mathbf{x_f} + \mathbf{P_f}\,\mathbf{u_f} \tag{A.8}$$

$$\mathbf{y_f} = \mathbf{K_f}\,\mathbf{x_f} \tag{A.9}$$

with $\lambda_{\mathrm{f}i}$, $i = 1 \ldots m_\mathrm{f}$, the poles of G_f and the matrix expressions:

$$\mathbf{J_f} = \begin{bmatrix} \lambda_{\mathrm{f}_1}\mathbb{I}_{n_\mathrm{f}} & \mathbf{0} & \ldots & \mathbf{0} \\ \mathbf{0} & \lambda_{\mathrm{f}_2}\mathbb{I}_{n_\mathrm{f}} & \ddots & \vdots \\ \vdots & \ddots & \ddots & \mathbf{0} \\ \mathbf{0} & \ldots & \mathbf{0} & \lambda_{\mathrm{f}_{m_\mathrm{f}}}\mathbb{I}_{n_\mathrm{f}} \end{bmatrix}, \quad \mathbf{P_f} = \begin{bmatrix} \mathbb{I}_{n_\mathrm{f}} \\ \mathbb{I}_{n_\mathrm{f}} \\ \vdots \\ \mathbb{I}_{n_\mathrm{f}} \end{bmatrix}, \tag{A.10}$$

$$\mathbf{K_f} = \begin{bmatrix} k_{\lambda_{\mathrm{f}_1}}\mathbb{I}_{n_\mathrm{f}} & k_{\lambda_{\mathrm{f}_2}}\mathbb{I}_{n_\mathrm{f}} & \ldots & k_{\lambda_{\mathrm{f}_{m_\mathrm{f}}}}\mathbb{I}_{n_\mathrm{f}} \end{bmatrix} \tag{A.11}$$

Then, the change of state variables $\mathbf{x}_{\mathbf{w_f}} = \mathbf{V}\,\mathbf{x_f}$, with $\mathbf{V} = \mathrm{blkdiag}(\mathbf{W_f}, \ldots, \mathbf{W_f}) \in \mathbb{R}^{m_\mathrm{f} n \times m_\mathrm{f} n_\mathrm{f}}$ is used to obtain the alternative model (20)-(21).

Appendix B. CDPR Linearization at a Steady State

The dynamics of a CDPR with elastic cables are obtained from (8) and the relationship between the cable

tensions and their elongations (27):

$$\mathbf{M}(\boldsymbol{x})\ddot{\boldsymbol{x}} + \mathbf{C}(\boldsymbol{x},\dot{\boldsymbol{x}})\dot{\boldsymbol{x}} + \mathbf{G_g} = \begin{bmatrix}\mathbf{W}_{\boldsymbol{\tau}}(\boldsymbol{x}) & \mathbf{W_f}(\boldsymbol{x})\end{bmatrix}\begin{bmatrix}\boldsymbol{\tau}(\boldsymbol{x},\mathbf{l_2})\\ \mathbf{f}\end{bmatrix} \tag{B.1}$$

$$\mathbf{y} = \begin{bmatrix}\boldsymbol{x}\\ \boldsymbol{\tau}\end{bmatrix} = \begin{bmatrix}\boldsymbol{x}\\ \mathbf{K_a}(\mathbf{l_2})[\mathbf{l_1}(\boldsymbol{x}) - \mathbf{l_2}]\end{bmatrix} \tag{B.2}$$

A linear model of the platform dynamics around a static equilibrium $\bar{\mathbf{x}}$ with $(\ddot{\boldsymbol{x}},\dot{\boldsymbol{x}},\boldsymbol{x},\mathbf{l_2},\mathbf{f}) = (\mathbf{0},\mathbf{0},\bar{\boldsymbol{x}},\bar{\mathbf{l}}_2,\mathbf{0})$ can be derived from a first-order Taylor expansion of (B.1)-(B.2). Let us define the pose, cable length, thrust and tension deviation variables with respect to the equilibrium state: $\boldsymbol{x}_\delta = \boldsymbol{x} - \bar{\boldsymbol{x}}$, $\mathbf{l}_{2\delta} = \mathbf{l_2} - \bar{\mathbf{l}}_2$, $\mathbf{f}_\delta = \mathbf{f}$ and $\boldsymbol{\tau}_\delta = \boldsymbol{\tau} - \bar{\boldsymbol{\tau}}$ with $\bar{\boldsymbol{\tau}} = \mathbf{K_a}(\bar{\mathbf{l}}_2)[\mathbf{l_1}(\bar{\boldsymbol{x}}) - \bar{\mathbf{l}}_2]$. Then, the output of the linear model is:

$$\mathbf{y}_\delta = \begin{bmatrix}\boldsymbol{x}_\delta\\ \boldsymbol{\tau}_\delta\end{bmatrix} = \begin{bmatrix}\boldsymbol{x}_\delta\\ \mathbf{T}_{\boldsymbol{x}}\,\boldsymbol{x}_\delta + \mathbf{T}_{\mathbf{l_2}}\,\mathbf{l}_{2\delta}\end{bmatrix} \tag{B.3}$$

with

$$\mathbf{T}_{\boldsymbol{x}} = \frac{\partial\boldsymbol{\tau}(\bar{\mathbf{x}})}{\partial\boldsymbol{x}} = -\mathbf{K_a}(\bar{\mathbf{l}}_2)\,\mathbf{W}_{\boldsymbol{\tau}}(\bar{\boldsymbol{x}})^{\mathrm{T}} \tag{B.4}$$

$$\mathbf{T}_{\mathbf{l_2}} = \frac{\partial\boldsymbol{\tau}(\bar{\mathbf{x}})}{\partial\mathbf{l_2}} = -\mathbf{K_a}(\bar{\mathbf{l}}_2) - \mathrm{diag}^{-1}(\bar{\mathbf{l}}_2)\,\mathrm{diag}(\bar{\boldsymbol{\tau}}) \tag{B.5}$$

The expression of $\mathbf{T}_{\boldsymbol{x}}$ derives from the relation $\frac{\partial\mathbf{l_1}(\boldsymbol{x})}{\partial\boldsymbol{x}} = -\mathbf{W}_{\boldsymbol{\tau}}(\boldsymbol{x})^{\mathrm{T}}$ between the wrench matrix (3) and the geometric Jacobian [34]. The derivation of $\mathbf{T}_{\mathbf{l_2}}$ expression is provided at the end of this appendix.

Based on the linear model of the tension (B.3), the Taylor expansion of the CDPR platform dynamics (B.1) yields:

$$\begin{aligned}\mathbf{M}(\bar{\boldsymbol{x}})\,\ddot{\boldsymbol{x}}_\delta =& \mathbf{W}_{\boldsymbol{\tau}}(\bar{\boldsymbol{x}})[\mathbf{T}_{\boldsymbol{x}}\,\boldsymbol{x}_\delta + \mathbf{T}_{\mathbf{l_2}}\,\mathbf{l}_{2\delta}] + \frac{\partial\mathbf{W}_{\boldsymbol{\tau}}(\bar{\boldsymbol{x}})}{\partial\boldsymbol{x}}\bar{\boldsymbol{\tau}}\,\boldsymbol{x}_\delta\\ &+ \mathbf{W_f}(\bar{\boldsymbol{x}})\,\mathbf{f} + \frac{\partial\mathbf{W_f}(\bar{\boldsymbol{x}})}{\partial\boldsymbol{x}}\bar{\mathbf{f}}\,\boldsymbol{x}_\delta\end{aligned} \tag{B.6}$$

where all the Jacobians of the Coriolis and centrifugal force are zero when evaluated for a static equilibrium ($\dot{\boldsymbol{x}} = \mathbf{0}$). Since $\bar{\mathbf{f}} = 0$, the last term of (B.6) vanishes and the linear model of the platform dynamics is:

$$\mathbf{M}(\bar{\boldsymbol{x}})\,\ddot{\boldsymbol{x}}_\delta + \mathbf{K}_{\boldsymbol{x}}\,\boldsymbol{x}_\delta = \begin{bmatrix}\mathbf{W}_{\boldsymbol{\tau}}(\bar{\boldsymbol{x}})\,\mathbf{T}_{\mathbf{l_2}} & \mathbf{W_f}(\bar{\boldsymbol{x}})\end{bmatrix}\begin{bmatrix}\mathbf{l}_{2\delta}\\ \mathbf{f}\end{bmatrix} \tag{B.7}$$

with the Cartesian stiffness matrix $\mathbf{K}_{\boldsymbol{x}}$:

$$\mathbf{K}_{\boldsymbol{x}} = -\mathbf{W}_{\boldsymbol{\tau}}(\bar{\boldsymbol{x}})\mathbf{T}_{\boldsymbol{x}} - \frac{\partial\mathbf{W}_{\boldsymbol{\tau}}(\bar{\boldsymbol{x}})}{\partial\boldsymbol{x}}\bar{\boldsymbol{\tau}} \tag{B.8}$$

From the linear model of the platform dynamics (B.7), the following liner model can be derived from the model (37) of the CDPR with its hybrid actuation dynamics:

$$\mathbf{M}(\bar{\boldsymbol{x}})\,\ddot{\boldsymbol{x}}_\delta + \mathbf{K}_{\boldsymbol{x}}\,\boldsymbol{x}_\delta = \begin{bmatrix}\mathbf{W}_{\boldsymbol{\tau}}\,\mathbf{T}_{\mathbf{l_2}}\,\mathbf{C}_{\mathbf{l_2}} & \mathbf{C_f}\end{bmatrix}\begin{bmatrix}\mathbf{x}_{\mathbf{l_2}\delta}\\ \mathbf{x}_{\mathbf{w_f}}\end{bmatrix} \tag{B.9}$$

$$\dot{\mathbf{x}}_{\mathbf{u}\delta} = \mathbf{A_u}\mathbf{x}_{\mathbf{u}\delta} + \mathbf{B_u}(\bar{\boldsymbol{x}})\begin{bmatrix}\dot{\mathbf{l}}_2^*\\ \mathbf{f}^*\end{bmatrix} \tag{B.10}$$

where the chain rule $\frac{\partial\boldsymbol{\tau}}{\partial\mathbf{x}_{\mathbf{i}_2}} = \frac{\partial\boldsymbol{\tau}}{\partial\mathbf{l}_2}\frac{\partial\mathbf{l}_2}{\partial\mathbf{x}_{\mathbf{i}_2}} = \frac{\partial\boldsymbol{\tau}}{\partial\mathbf{l}_2}\mathbf{C}_{\mathbf{l_2}}$ is used and $\mathbf{x}_{\mathbf{u}\delta} = \mathbf{x_u} - \bar{\mathbf{x}}_{\mathbf{u}}$ is the vector of the actuation state deviations from the static equilibrium $\bar{\mathbf{x}}$.

Thereby, a discrete-time state-space representation of the augmented model $\boldsymbol{f}_{\mathbf{aug}}$ (47)-(49) linearized around a static equilibrium is:

$$\begin{aligned}\mathbf{x}_{\delta_{k+1}} = \mathbf{x}_{\delta_k} &+ \Delta t\begin{bmatrix}\mathbf{0} & -\mathbf{M}^{-1}\mathbf{K}_{\boldsymbol{x}} & \mathbf{0} & \mathbf{M}^{-1}\mathbf{W}_{\boldsymbol{\tau}}\mathbf{T}_{\mathbf{l_2}}\mathbf{C}_{\mathbf{l_2}} & \mathbf{M}^{-1}\mathbf{C_f}\\ \mathbb{I}_n & \mathbf{0} & \mathbf{0} & \mathbf{0} & \mathbf{0}\\ \mathbf{0} & \mathbf{0} & \mathbf{0} & \mathbf{0} & \mathbf{0}\\ \mathbf{0} & \mathbf{0} & \mathbf{B}_{\mathbf{l_2}} & \mathbf{A}_{\mathbf{l_2}} & \mathbf{0}\\ \mathbf{0} & \mathbf{0} & \mathbf{0} & \mathbf{0} & \mathbf{A_f}\end{bmatrix}\mathbf{x}_{\delta_k}\\ &+\Delta t\begin{bmatrix}\mathbf{0} & \mathbf{0}\\ \mathbf{0} & \mathbf{0}\\ \mathbb{I}_{n_\tau} & \mathbf{0}\\ \mathbf{0} & \mathbf{0}\\ \mathbf{0} & \mathbf{B_f}\mathbf{W_f}(\bar{\boldsymbol{x}})\end{bmatrix}\mathbf{u}_k + \Delta t\begin{bmatrix}\mathbf{M}^{-1}\\ \mathbf{0}\\ \mathbf{0}\\ \mathbf{0}\\ \mathbf{0}\end{bmatrix}\mathbf{d}_k\end{aligned} \tag{B.11}$$

$$\mathbf{y}_{\delta_k} = \begin{bmatrix}\mathbf{0} & \mathbb{I}_n & \mathbf{0} & \mathbf{0} & \mathbf{0}\\ \mathbf{0} & \mathbf{T}_{\boldsymbol{x}} & \mathbf{0} & \mathbf{T}_{\mathbf{l_2}}\mathbf{C}_{\mathbf{l_2}} & \mathbf{0}\end{bmatrix}\mathbf{x}_{\delta_k} \tag{B.12}$$

Derivation of $\mathbf{T}_{\mathbf{l_2}}$ *expression.*

$$\begin{aligned}&\frac{\partial\mathbf{K_a}(\bar{\mathbf{l}}_2)}{\partial\mathbf{l_2}}[\mathbf{l_1}(\bar{\boldsymbol{x}}) - \bar{\mathbf{l}}_2] = \frac{\partial\mathrm{diag}^{-1}(\bar{\mathbf{l}}_2)}{\partial\mathbf{l_2}}\mathrm{diag}(k_{s_i})[\mathbf{l_1}(\bar{\boldsymbol{x}}) - \bar{\mathbf{l}}_2]\\ &= -\mathrm{diag}^{-1}(\bar{\mathbf{l}}_2)\,\frac{\partial\mathrm{diag}(\bar{\mathbf{l}}_2)}{\partial\mathbf{l_2}}\mathrm{diag}^{-1}(\bar{\mathbf{l}}_2)\mathrm{diag}(k_{s_i})[\mathbf{l_1}(\bar{\boldsymbol{x}}) - \bar{\mathbf{l}}_2]\\ &= -\mathrm{diag}^{-1}(\bar{\mathbf{l}}_2)\,\frac{\partial\mathrm{diag}(\bar{\mathbf{l}}_2)}{\partial\mathbf{l_2}}\,\underbrace{\mathbf{K_a}(\bar{\mathbf{l}}_2)[\mathbf{l_1}(\bar{\boldsymbol{x}}) - \bar{\mathbf{l}}_2]}_{\bar{\boldsymbol{\tau}}}\\ &= -\mathrm{diag}^{-1}(\bar{\mathbf{l}}_2)\,\mathrm{diag}(\bar{\boldsymbol{\tau}})\end{aligned} \tag{B.13}$$

using the identity $\frac{\partial\mathbf{A}^{-1}}{\partial u} = -\mathbf{A}^{-1}\frac{\partial\mathbf{A}}{\partial u}\mathbf{A}^{-1}$. Thereby,

$$\mathbf{T}_{\mathbf{l_2}} = \frac{\partial\boldsymbol{\tau}}{\partial\mathbf{l_2}} = \mathbf{K_a}(\bar{\mathbf{l}}_2)\frac{\partial[\mathbf{l_1}(\bar{\boldsymbol{x}}) - \mathbf{l_2}]}{\partial\mathbf{l_2}} + \frac{\partial\mathbf{K_a}(\bar{\mathbf{l}}_2)}{\partial\mathbf{l_2}}[\mathbf{l_1}(\bar{\boldsymbol{x}}) - \bar{\mathbf{l}}_2] \tag{B.14}$$

$$= -\mathbf{K_a}(\bar{\mathbf{l}}_2) - \mathrm{diag}^{-1}(\bar{\mathbf{l}}_2)\,\mathrm{diag}(\bar{\boldsymbol{\tau}}) \tag{B.15}$$

Appendix C. Supplementary Material

A video of the experiments with the PiSaRo4 CDPR and its hybrid cable-thruster actuation is available with this article.

Declaration of competing interest

The authors declare that they have no known competing financial interests or personal relationships that could have appeared to influence the work reported in this paper.

Acknowledgements

This work was supported by the e-VISER project funded by the French National Research Agency (ANR-17-CE33-0008).

The authors would like to thank Yannick Kuhn, M. Eng., for his work on the experimental setup and for the preliminary experiments with the PiSaRo4 robot.

References

[1] X. Tang, An Overview of the Development for Cable-Driven Parallel Manipulator, Advances in Mechanical Engineering 6 (2014).

[2] P. Bosscher, A. Riechel, I. Ebert-Uphoff, Wrench-feasible workspace generation for cable-driven robots, IEEE Transactions on Robotics 22 (2006) 890–902.

[3] M. Gouttefarde, J. Lamaury, C. Reichert, T. Bruckmann, A versatile tension distribution algorithm for n -dof parallel robots driven by $n+2$ cables, IEEE Transactions on Robotics 31 (2015) 1444–1457.

[4] S.-R. Oh, S. Agrawal, Cable suspended planar robots with redundant cables: controllers with positive tensions, IEEE Transactions on Robotics 21 (2005) 457–465.

[5] S. Kawamura, W. Choe, S. Tanaka, S. Pandian, Development of an ultrahigh speed robot FALCON using wire drive system, in: Proceedings of 1995 IEEE International Conference on Robotics and Automation, volume 1, 1995, pp. 215–220 vol.1.

[6] L. Cuvillon, X. Weber, J. Gangloff, Modal Control for Active Vibration Damping of Cable-Driven Parallel Robots, Journal of Mechanisms and Robotics 12 (2020).

[7] D. W. Robinson, J. E. Pratt, D. J. Paluska, G. A. Pratt, Series elastic actuator development for a biomimetic walking robot, in: 1999 IEEE/ASME International Conference on Advanced Intelligent Mechatronics (Cat. No.99TH8399), 1999, pp. 561–568.

[8] M. Seo, S. Yoo, M. Choi, J. Oh, H. S. Kim, T. Seo, Vibration Reduction of Flexible Rope-Driven Mobile Robot for Safe Façade Operation, IEEE/ASME Transactions on Mechatronics 26 (2021) 1812–1819.

[9] H. Hussein, J. C. Santos, M. Gouttefarde, Geometric Optimization of a Large Scale CDPR Operating on a Building Facade, in: 2018 IEEE/RSJ International Conference on Intelligent Robots and Systems (IROS), 2018, pp. 5117–5124.

[10] R. Thompson, M. Blackstone, Three-dimensional moving camera assembly with an informational cover housing, 2005. US Patent 6,873,355.

[11] M. A. Khosravi, H. D. Taghirad, Dynamic modeling and control of parallel robots with elastic cables: Singular perturbation approach, IEEE Transactions on Robotics 30 (2014) 694–704.

[12] H. Jamshidifar, S. Khosravani, B. Fidan, A. Khajepour, Vibration decoupled modeling and robust control of redundant cable-driven parallel robots, IEEE/ASME Transactions on Mechatronics 23 (2018) 690–701.

[13] J. Begey, L. Cuvillon, M. Lesellier, M. Gouttefarde, J. Gangloff, Dynamic control of parallel robots driven by flexible cables and actuated by position-controlled winches, IEEE Transactions on Robotics 35 (2018) 286–293.

[14] R. J. Caverly, J. R. Forbes, Dynamic modeling and noncollocated control of a flexible planar cable-driven manipulator, IEEE Transactions on Robotics 30 (2014) 1386–1397.

[15] X. Weber, L. Cuvillon, J. Gangloff, Active vibration canceling of a cable-driven parallel robot using reaction wheels, in: 2014 IEEE/RSJ International Conference on Intelligent Robots and Systems, IEEE, 2014, pp. 1724–1729.

[16] M. Lesellier, L. Cuvillon, J. Gangloff, M. Gouttefarde, An active stabilizer for cable-driven parallel robot vibration damping, in: 2018 IEEE/RSJ International Conference on Intelligent Robots and Systems (IROS), IEEE, 2018, pp. 5063–5070.

[17] R. Qi, M. Rushton, A. Khajepour, W. W. Melek, Decoupled modeling and model predictive control of a hybrid cable-driven robot (hcdr), Robotics and Autonomous Systems 118 (2019) 1–12.

[18] H. Jamshidifar, M. Rushton, A. Khajepour, A Reaction-Based Stabilizer for Nonmodel-Based Vibration Control of Cable-Driven Parallel Robots, IEEE Transactions on Robotics 37 (2021) 667–674.

[19] H. Sellet, I. Khayour, L. Cuvillon, S. Durand, J. Gangloff, Active Damping of Parallel Robots Driven by Flexible Cables Using Cold-Gas Thrusters, in: 2019 International Conference on Robotics and Automation (ICRA), 2019, pp. 530–536.

[20] Y. Sun, M. Newman, A. Zygielbaum, B. Terry, Active vibration damping of a cable-driven parallel manipulator using a multirotor system, in: A. Pott, T. Bruckmann (Eds.), Cable-Driven Parallel Robots, Springer International Publishing, 2019, pp. 403–414.

[21] Y. S. Sarkisov, M. J. Kim, D. Bicego, D. Tsetserukou, C. Ott, A. Franchi, K. Kondak, Development of SAM: cable-Suspended Aerial Manipulator, in: 2019 International Conference on Robotics and Automation (ICRA), 2019, pp. 5323–5329.

[22] I. Khayour, L. Cuvillon, C. Butin, A. Yiğit, S. Durand, J. Gangloff, Improving Disturbance Rejection and Dynamics of Cable Driven Parallel Robots with On-board Propellers, in: 2020 IEEE/RSJ International Conference on Intelligent Robots and Systems (IROS), 2020, pp. 6564–6569.

[23] K. Seo, S. Cho, T. Kim, H. S. Kim, J. Kim, Design and stability analysis of a novel wall-climbing robotic platform (ROPE RIDE), Mechanism and Machine Theory 70 (2013) 189–208.

[24] A. Yiğit, M. A. Perozo, L. Cuvillon, S. Durand, J. Gangloff, Novel Omnidirectional Aerial Manipulator With Elastic Suspension: Dynamic Control and Experimental Performance Assessment, IEEE Robotics and Automation Letters 6 (2021) 612–619.

[25] Z. Li, J. Erskine, S. Caro, A. Chriette, Design and Control of a Variable Aerial Cable Towed System, IEEE Robotics and Automation Letters 5 (2020) 636–643.

[26] G. El-Ghazaly, M. Gouttefarde, V. Creuze, Hybrid cable-thruster actuated underwater vehicle-manipulator systems: A study on force capabilities, in: 2015 IEEE/RSJ International Conference on Intelligent Robots and Systems (IROS), 2015, pp. 1672–1678.

[27] Y. Sun, Y. Guo, C. Song, D. Lau, Wrench-feasible workspace-based design of hybrid thruster and cable driven parallel robots,

Mechanism and Machine Theory 172 (2022) 104758.
[28] T. A. Johansen, T. I. Fossen, Control allocation—a survey, Automatica 49 (2013) 1087 – 1103.
[29] Yu Luo, A. Serrani, S. Yurkovich, D. B. Doman, M. W. Oppenheimer, Model predictive dynamic control allocation with actuator dynamics, in: Proceedings of the 2004 American Control Conference, volume 2, 2004, pp. 1695–1700 vol.2.
[30] A. Veksler, T. A. Johansen, F. Borrelli, B. Realfsen, Dynamic positioning with model predictive control, IEEE Transactions on Control Systems Technology 24 (2016) 1340–1353.
[31] C. Song, D. Lau, Workspace-Based Model Predictive Control for Cable-Driven Robots, IEEE Transactions on Robotics (2022) 1–20.
[32] J. C. Santos, M. Gouttefarde, A. Chemori, A Nonlinear Model Predictive Control for the Position Tracking of Cable-Driven Parallel Robots, IEEE Transactions on Robotics (2022) 1–20.
[33] M. Morari, U. Maeder, Nonlinear offset-free model predictive control, Automatica 48 (2012) 2059–2067.
[34] B. Siciliano, L. Sciavicco, L. Villani, G. Oriolo, Robotics: Modelling, Planning and Control, Advanced Textbooks in Control and Signal Processing, Springer London, London, 2009.
[35] K. Ogata, Modern control engineering, Prentice-Hall electrical engineering series. Instrumentation and controls series, 5th ed ed., Prentice-Hall, Boston, 2010.
[36] G. Meunier, B. Boulet, M. Nahon, Control of an overactuated cable-driven parallel mechanism for a radio telescope application, IEEE Transactions on Control Systems Technology 17 (2009) 1043–1054.
[37] J. A. Rossiter, Model-based predictive control: a practical approach, Control series, CRC Press, Boca Raton, 2003.
[38] U. Maeder, F. Borrelli, M. Morari, Linear offset-free Model Predictive Control, Automatica 45 (2009) 2214–2222.
[39] M. Gouttefarde, D. Daney, J.-P. Merlet, Interval-analysis-based determination of the wrench-feasible workspace of parallel cable-driven robots, IEEE Transactions on Robotics 27 (2010) 1–13.
[40] R. Verschueren, G. Frison, D. Kouzoupis, J. Frey, N. v. Duijkeren, A. Zanelli, B. Novoselnik, T. Albin, R. Quirynen, M. Diehl, acados—a modular open-source framework for fast embedded optimal control, Mathematical Programming Computation 14 (2022) 147–183.
[41] G. Strang, Linear algebra and its applications, Thomson, Brooks/Cole, Belmont, CA, 2006.
[42] G. Pannocchia, M. Gabiccini, A. Artoni, Offset-free MPC explained: Novelties, subtleties, and applications, IFAC-PapersOnLine 48 (2015) 342–351.
[43] D. Wang, J. Ahn, J. Jung, J.-A. Seon, J.-O. Park, S. Y. Ko, S. Park, Winch-integrated mobile end-effector for a cable-driven parallel robot with auto-installation, International Journal of Control, Automation and Systems 15 (2017) 2355–2363.
[44] S. Yoo, T. Kim, M. Seo, J. Oh, J. Kim, H. S. Kim, T. Seo, Modeling and verification of multi-winding rope winch for facade operation, Mechanism and Machine Theory 155 (2021) 104105.
[45] X. Jiang, C. Gosselin, Trajectory Generation for Three-Degree-of-Freedom Cable-Suspended Parallel Robots Based on Analytical Integration of the Dynamic Equations, Journal of Mechanisms and Robotics 8 (2016).
[46] J. Garus, Optimization of Thrust Allocation in Propulsion System of Underwater Vehicle, Int. J. Appl. Math. Comput. Sci 14 (2004) 461–467.
[47] D. M. Lima, J. E. Normey-Rico, T. L. M. Santos, Robust delay compensation for MPC for systems with input nonlinearities and multiple dead times, in: 2016 IEEE Conference on Control Applications (CCA), 2016, pp. 1362–1367.